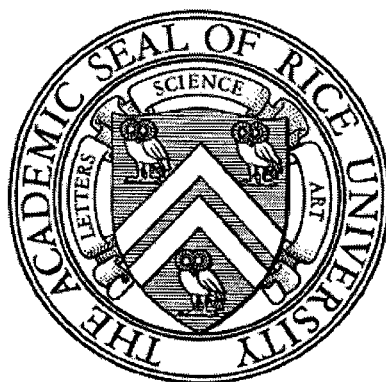


RICE UNIVERSITY



Charge Regulation in Lipid Membranes due to Lipid Mobility

by

Yantrawaduge Nissanka Sirimevan Wickremasinghe

DOCTOR OF PHILOSOPHY

HOUSTON, TEXAS

June 2009

UMI Number: 3421327

All rights reserved

INFORMATION TO ALL USERS

The quality of this reproduction is dependent upon the quality of the copy submitted.

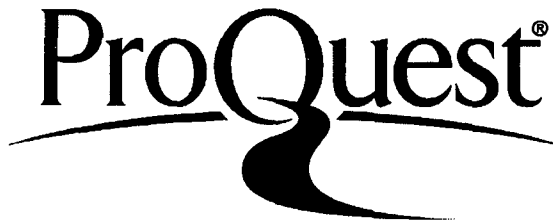
In the unlikely event that the author did not send a complete manuscript and there are missing pages, these will be noted. Also, if material had to be removed, a note will indicate the deletion.



UMI 3421327

Copyright 2010 by ProQuest LLC.

All rights reserved. This edition of the work is protected against unauthorized copying under Title 17, United States Code.



ProQuest LLC
789 East Eisenhower Parkway
P.O. Box 1346
Ann Arbor, MI 48106-1346

RICE UNIVERSITY

Charge Regulation in Lipid Membranes due to Lipid Mobility

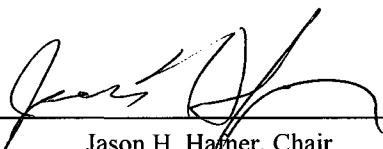
by

Yantrawaduge Nissanka Sirimevan Wickremasinghe

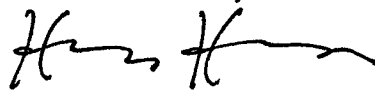
A THESIS SUBMITTED
IN PARTIAL FULFILLMENT OF THE
REQUIREMENTS FOR THE DEGREE

Doctor of Philosophy


APPROVED, THESIS COMMITTEE:



Jason H. Hagner, Chair
Associate Professor of Physics and Astronomy
and Chemistry



Huey W. Huang
Professor of Physics and Astronomy



Yousif Shamoo
Associate Professor of Biochemistry and Cell Biology

HOUSTON, TEXAS

June 2009

Abstract

CHARGE REGULATION IN LIPID MEMBRANES DUE TO LIPID MOBILITY

by

Yantrawaduge Nissanka Sirimevan Wickremasinghe

Lipid bilayer membranes are ubiquitous in biology and electrostatics play a key role in their functionality. The interfacial electrostatics of lipid bilayers involves interplay between the surface potential and charge regulation in the form of ion binding, protonation and lipid mobility. Mobile lipid charge regulation in particular is unique to lipid interfaces and is thought to be an important factor in charged macromolecule-membrane interactions. We used Atomic Force Microscopy (AFM) for the first nanometer scale experimental demonstration of mobile lipid charge regulation occurring in supported lipid bilayer membranes. By combining finite element computer simulations and experimental AFM data, we showed that mobile lipid charge regulation accounts for the short range deviations from the expected electrostatics over anionic lipids. We also accounted for van der Waal interactions and electrolyte ion binding in our calculations and found the mobility of the lipid to be the dominant factor in the short range deviations. Control experiments on silicon nitride surfaces, whose surface charges are immobile, showed that the short range deviation could be accounted for by the formation of a stern layer due to cation binding. Further evidence for tip-induced mobile lipid charge regulation was presented in the form of clear differences in the short range electrostatics of mobile fluid phase lipids when compared to immobile gel phase lipids. Furthermore, our data confirmed the theoretically predicted differences between surfaces containing mobile versus immobile charges.

Acknowledgements

First, I would like to thank my adviser Dr. Jason Hafner for guiding me through the long and difficult process that is the Ph.D. I am eternally grateful for his patient mentoring. Thanks also go out to my committee members Dr. Huey Huang and Dr. Yousif Shamoo for giving of their time. I would also especially like to thank Dr. Clayton Simien for the support he provided at various times. I would also like to especially thank my lab-mate Dr. Yi Yang and Kathryn Mayer for their scientific input and well as for being such a joy to work with. Also, thanks go out to my colleagues Dr. Colleen Nehl and Dr. Hongwei Liao and Sean Lee who were helpful to me in many different ways during my graduate career. I also thank my friends from Rice, Luke Probst, Chris Ralston, Dr. Sarah Nagel, Natali Martinez, Dr. Christine Peebles, Dr. Vinay Ribeiro, Dr. Paul Fortunato, Mike Karim and all the others from RGCF who were a great support to me. Thanks also to the people from WUBC, Roger Patterson, Erik Lawrence, Dave Allee, Jim and Shireen Tour and many others who made me feel welcome. I am eternally grateful to Emilia for her love and support as well as her scientific input. Finally, I would like to thank my parents and my sisters for teaching me right from wrong and for giving me the opportunity to follow my dreams and for teaching me right from wrong. I dedicate this to the memory of my father who gave so much of himself so that we, his children could prosper.

Table of Contents

Abstract		iii
Acknowledgements		iv
List of Figures		vii
Chapter 1	Introduction	
	1.1 Scope and layout of this thesis	1
	1.2 Lipid bilayer membranes	1
	1.3 Membrane electrostatics	4
	1.4 Atomic Force Microscopy	6
	1.5 Membrane electrostatics with AFM	9
	1.6 Electrostatic double layer force and charge regulation	11
	1.7 Charge regulation at lipid interfaces	12
Chapter 2	Quantitative Membranes electrostatics with AFM	
	2.1 Introduction	13
	2.2 Materials and methods	
	2.2.1 Preparation of DOPC:DOPS supported lipid membranes	15
	2.2.2 Force curve acquisition and analysis	16
	2.2.3 Tip charge density measurement	17
	2.2.4 Tip radius and spring constant measurement	18
	2.2.4 Finite Element Modeling	18

2.3 Results and discussion	22
Chapter 3 Mobile Lipid Charge Regulation in Membranes	
3.1 Introduction	26
3.2 Experimental method	
3.2.1 Preparation of DOPC:DOPS supported lipid membranes	29
3.2.2 Preparation of DOPC:DOPS:DMPC:DMPS supported lipid membranes	30
3.2.3 Computational analysis	31
3.3 Results	
3.3.1 Van der Waals interaction	34
3.3.2 Charge regulation due to counterion binding; lipid vs. silicon nitride	35
3.3.3 Mobile lipid charge regulation	39
3.3.4 Comparing mobile lipid charge regulation on gel and fluid phase lipids	41
3.4 Discussion	47
References	51

List of Figures

- Figure 1.1** 2
Structure of a Phospholipid molecule. The head group is hydrophilic. The tail group is comprised of an oily fatty acid group and is thus hydrophobic. The average lipid molecule is on the order of 2 nm in length.
- Figure 1.2** 3
(a) Self assembly of lipids into cell membranes. (b) Schematic diagram of an animal cell denoting some of its components.
- Figure 1.3** 3
Representation of a cellular membrane. In addition to lipid molecules, it also contains proteins, carbohydrates and ion channels. It is also supported by the cells cytoskeleton. (Public domain image)
- Figure 1.4** 5
An illustration of the three membrane potentials. The transmembrane potential (ψ_{tr}), the surface potential (ψ_s) and the dipole potential (ψ_d).
- Figure 1.5** 6
Schematic of typical AFM tip-cantilever assemblies. Schematic of typical AFM tip-cantilever assemblies.
- Figure 1.6** 7
(Left) Schematic of an AFM optical detection system; a laser is bounced off the back of the AFM tip and directed to a split photodiode. (Right) Scanning Electron Microscope image of an AFM tip.
- Figure 1.7** 8
AFM image of an IgM antibody (image is approximately 20 nm x 20 nm in size). Image taken from Reference [13].
- Figure 1.8** 9
Schematic of a typical AFM force-distance curve showing both approach and retract curves. Image taken from Reference [16].
- Figure 1.9** 10
Schematic of supported lipid bilayer preparation by vesicle fusion. When preformed lipid vesicles are exposed to a flat substrate (mica in the above case), they rupture and form supported lipid bilayers.

Figure 1.10	11
Schematic of the diffuse electric double layer formed over a negatively charged surface. The red dots represent positive counterions. The density of the counterions close to the surface is higher than in the bulk. This cloud of positive counterions is the diffuse electric double layer.	
Figure 2.1	19
(Top Left) 3D schematic diagram, (Top Right) Finite Element Domains I to IV, not to scale. (Bottom) Portion of the mesh generated while solution is computed.	
Figure 2.2	22
The lipid membrane charge densities determined by applying Equation 2.1 to the experimental force curves. The data do not follow the expected trend with DOPS mole fraction.	
Figure 2.3	23
Comparing data and simulation results. Each solid, colored line represents the computationally simulated force curve obtained by using various guesses as to the lipid surface charge density. Note that the data is fit to the model only in the long-range region (1–4 Debye lengths).	
Figure 2.4	24
(a) Lipid membrane charge densities and, (b) surface potentials determined by a numerical analysis of the experimental force curves. The data (squares) follow the curves predicted by the Gouy-Chapman-Stern model (line).	
Figure 3.1	27
Schematic of AFM tip-induced mobile charge regulation. Neutral lipids are shown in yellow and the anionic lipids are shown in white. (a) In an unperturbed lipid bilayer, the neutral and the anionic lipids are distributed homogeneously. (b) The close proximity of the negatively charged AFM tip induces the negative lipid molecules to move away and results in a patch of mostly neutral lipids forming underneath the AFM tip.	
Figure 3.2	28
(a) The fixed charged density model is a good fit for the data for $D > 11$ nm. (b) A closer view of the same data shown in (a) reveals that the simulation deviates from the data when $D < 11$ nm. The data is for a 1:5, DOPC:DOPS mixture.	
Figure 3.3	31
Fluid AFM topography image of a 1:9, DMPC:DMPS lipid patch. We are able to identify the lipid bilayer patch from its cross-sectional height which is 5nm. The scan size is 1x1 μ m.	

Figure 3.4	32
<p>(Left) The finite element model is solved with a constant charge density boundary condition from $D = 40$ nm to $D = 11$ nm as in Chapter 2. Note that these values of D are for the data shown in Figure 3.2. For other data sets, the D values will be different. For $D = 11$ nm and less, we vary the lipids surface charge density according to the law governing the phenomenon being addressed (i.e. whether it is counterion binding or mobile lipid charge regulation).</p>	
Figure 3.5	32
<p>D_0 is chosen as the point where the AFM data starts deviating significantly from the electrostatic simulation of Chapter 2. For the above sample, $D_0 = 11$ nm. The AFM data and the electrostatic simulation shown here is the same as in Figure 3.2.</p>	
Figure 3.6	33
<p>Schematic of how the tip-induced charge regulation finite element model is implemented. Here, ψ is the surface potential σ is the surface charge density of the lipid bilayer and F is the electrostatic force on the tip. The functional form of g will depend on the form of charge regulation being considered (e.g. charge regulation due to counterion binding).</p>	
Figure 3.7	35
<p>Comparison of the AFM data with the van der Waals computational model. The AFM data and the electrostatic simulation shown here are the same as in Figure 3.2.</p>	
Figure 3.8	37
<p>Comparison of the AFM data with the van der Waals and stern layer inclusive computational model. The AFM data and the electrostatic simulation shown here is the same as in Figure 3.2.</p>	
Figure 3.9	38
<p>AFM data for a Si_3N_4 sample fit with a model that includes charge regulation due to cation binding via a Langmuir isotherm. (Black, solid curve) - AFM data, (Red, dashed curve) - constant surface charge electrostatic model, (Blue, solid curve) - cation binding model.</p>	
Figure 3.10	40
<p>Data fit with the Boltzmann relaxation model of mobile lipid charge regulation. The AFM data and the electrostatic simulation shown here is the same as in Figure 3.2.</p>	
Figure 3.11	42
<p>(Top) DOPC-neutral at pH 7, (Bottom) DOPS-anionic. A mixture of these lipids will be in fluid phase at room temperature.</p>	

- Figure 3.12** 42
 (Top) DMPC-neutral at pH 7, (Bottom) DMPS-anionic. A mixture of these lipids will be in fluid phase at room temperature.
- Figure 3.13** 43
 Schematic of gel phase (Blue) and fluid phase (Yellow) lipid bilayers coexisting. The gel phase lipid regions are more rigidly packed and are thicker than the loosely packed fluid phase lipid regions.
- Figure 3.14** 43
 AFM imaging data of the DOPC:DOPS:DMPC:DMPS mixture. (Left) Topography of the lipid mix, the lighter colors represent taller features - the image is 1x1 μm in size. (Right) A cross section taken through the topographical image – as shown by the white line. The height difference between the lighter and the darker areas is 0.8 nm, identifying the lighter regions as gel phase patches residing in a sea of fluid phase lipid sea.
- Figure 3.15** 44
 Schematic of Fluid Electric Force Microscopy (FEFM). The force F experienced by the tip during the lift scan is directly proportional to the samples surface charge density σ_{sample} .
- Figure 3.16** 45
 AFM topography image of a 1:9, DMPC:DMPS lipid patch. (Left) Topographic image of the lipid bilayer. (Right) Charge map of the same area showing the charge contrast between the lipid and the mica. The scan size is 1x1 μm .
- Figure 3.17** 45
 FEFM imaging of the DOPC:DOPS:DMPC:DMPS mixture. (Left) Topography of the lipid mix, the lighter colors represent taller features. (Right) The charge map of the same region showing no discernable charge contrast. The scan size is 2 x 2 μm .
- Figure 3.18** 46
 Comparison of force curves taken over fluid phase (Blue curve) and gel phase (Red curve) shown with a constant surface charge electrostatic fit (Black dashed curve). Both sets of data were taken with the same tip during the same experiment and the electrostatic fit was obtained for a surface charge density of -0.04 C/m^2 .

Figure 3.19

From Reference [26]. Theoretical prediction of a DNA–membrane interaction for three different models of a membrane. The DNA was modeled as a charged cylinder of length L and radius r_0 . $\beta\Omega$ is the grand potential and τ is the line charge density and h is the distance from lipid surface to center of cylinder. In the above, the quantity plotted on the y-axis is electrostatic interaction energy between the cylinder and the surface and the quantity plotted on the x-axis is related to the DNA-membrane separation. (*mobile*): the model membrane is composed of three types of mobile surface groups: negatively charged, neutral and dissociable. (*N-P*): membrane charges result from dissociation as in case I, but surface ions are immobile. (*homogeneous*): charges are fixed, surface ions are immobile. In all three cases, the homogeneous surface charge density far away from the DNA is equal and corresponds to an effective homogeneous charge density of $\rho_c = -1/4.8 \text{ nm}^2$ ($\kappa^{-1} = 50 \text{ nm}$).

Chapter 1

Introduction

1.1 Scope and layout of this thesis

This thesis presents a study of interfacial lipid membrane electrostatics using atomic force Microscopy (AFM). The specific problem described and solved herein is the experimental observation of charge regulation due to the mobility of lipids. Chapter 1 of this thesis introduces the lipid bilayer membrane and discusses its importance in a biological context-specifically focusing on the electrostatics of the membrane. Chapter 1 also gives an overview of biological AFM and of its usage in the study of membrane electrostatics in particular. Chapter 2 of this thesis reviews previous work [1] on using AFM in quantitative membrane electrostatics and discusses the limitations of that work. Chapter 2 provides context for and is the starting point of the original work performed in Chapter 3. In addition to extending the methods used in the preceding chapter, Chapter 3 presents the first experimental observation of mobile lipid charge regulation.

1.2 Lipid bilayer membranes

Lipid bilayer membranes form the boundary of many biological entities such as cells, organelles and viruses. These membranes are on the order of 5 nm in transverse thickness and can range up to many microns laterally. Lipid membranes are highly impervious to aqueous soluble molecules and ions, and therefore form a dynamic barrier between the

biological entity and the exterior. For cells, the membrane plays a role in maintaining interior salt concentrations and pH at appropriate values. The key components of a cellular membrane are the lipid molecules. Lipids are characterized by a hydrophilic (polar) head group and a hydrophobic (non-polar) tail group. This amphipathic nature results in self-assembly into the lipid bilayer structures seen in cells.

A given biological membrane will be composed of a number of different types of these lipids. Cell membranes in particular are composed of phospholipids.

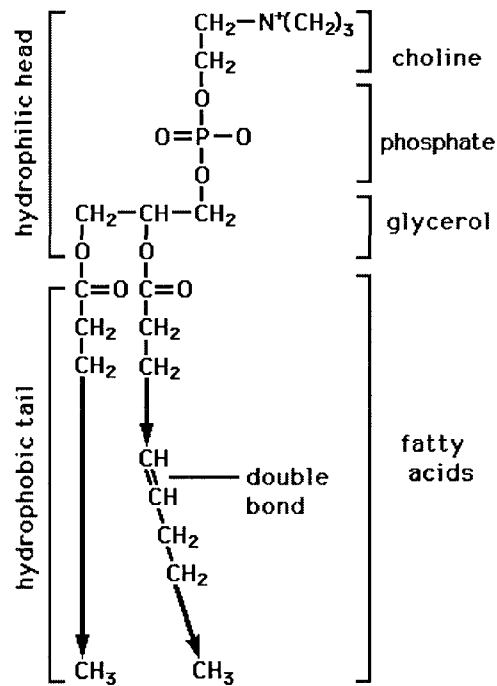


Figure 1.1: Structure of a Phospholipid molecule. The head group is hydrophilic. The tail group is comprised of an oily fatty acid group and is thus hydrophobic. The average lipid molecule is on the order of 2 nm in length.

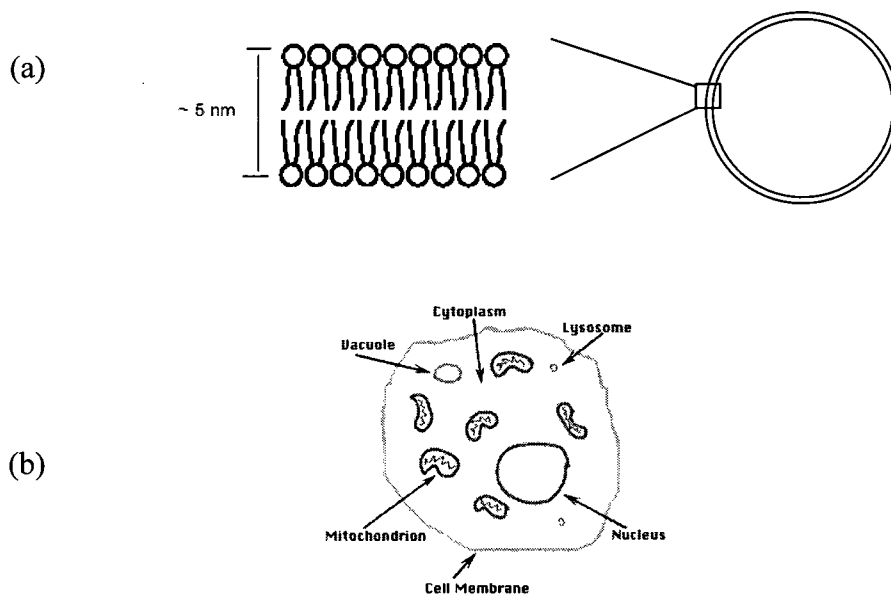


Figure 1.2: (a) Self assembly of lipids into cell membranes. (b) Schematic diagram of an animal cell denoting some of its components.

In addition to the lipid molecules, the cellular membrane also contains a diverse variety of other molecules such as proteins and carbohydrates. These various molecules act in concert with the lipids to perform the various functions of the biomembrane.

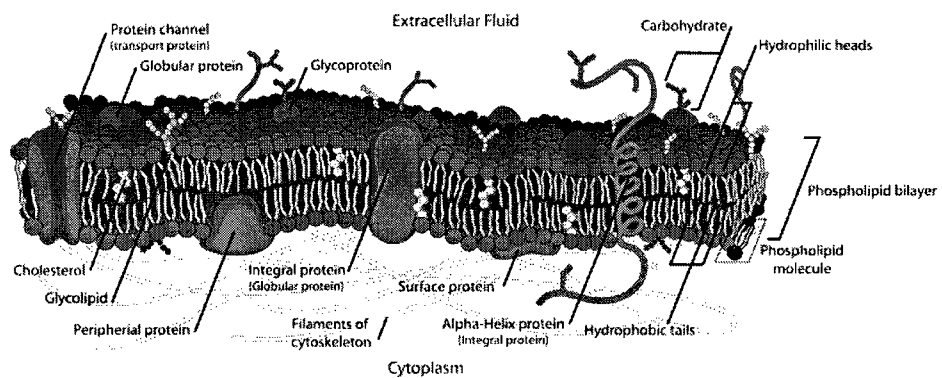


Figure 1.3: Representation of a cellular membrane. In addition to lipid molecules, it also contains proteins, carbohydrates and ion channels. It is also supported by the cells cytoskeleton. (Public domain image)

For example, certain types of membrane proteins allow cells to identify and interact with each other. Other types of membrane proteins regulate the transport of ions and other molecules across the membrane. Membrane functionality is mediated by a complex array of interactions including mechanical, hydrophobic and electrostatic. In this thesis we will focus on the electrostatic aspects of these membranes.

1.3 Membrane electrostatics

Many different types of lipid species found in biological membranes carry net charges at physiological pH values. These charged lipids result in the presence of various surface potentials that are different from the potential of the bulk electrolyte. Thus, the concentration profiles of ions close to the lipid surface is a lot more complicated than that of the bulk [2]. These charged lipids are instrumental in electrostatic membrane interactions. The electrostatic interactions near and around the membrane are characterized by three potentials, illustrated in Figure 1.4. The transmembrane potential (ψ_{tr}), drives ion transport through channels in cell membranes, a basic step in many biological processes [3]. The surface potential (ψ_s) regulates the interaction of cytosolic and environmental factors with cell membranes [4]. These two potentials are well studied and have clearly demonstrable effects on membrane function. The third membrane potential, known as the dipole potential (ψ_d) however yet to be conclusively characterized, this is a relatively large potential barrier (~100's of mV across a 5 nm spacing) at the membrane midplane created by inward-pointing molecular dipoles at the interfacial planes [5].

The dipole potential has been linked to biological functions such as protein adsorption and insertion into membranes [6, 7], as well as effects of anesthetics [8].

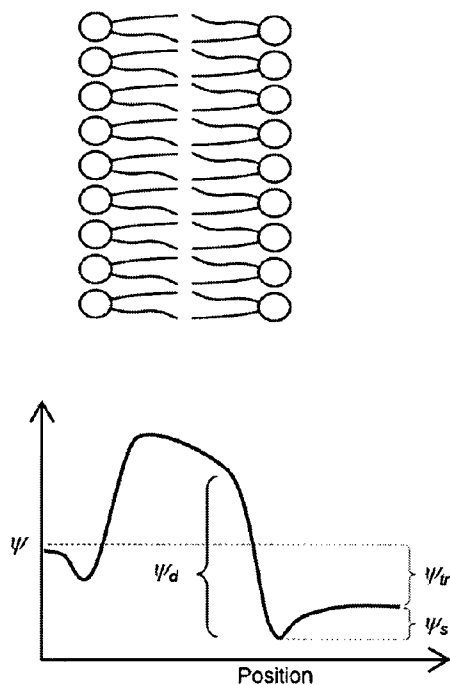


Figure 1.4: An illustration of the three membrane potentials. The transmembrane potential (ψ_{tr}), the surface potential (ψ_s) and the dipole potential (ψ_d).

In order to accurately describe the electrostatics of membrane function it would be necessary to fully characterize the potentials throughout the membrane. Such a characterization is impeded by the complexity of the environment with its host of ions, water molecules in an area of high dielectric anisotropy. Such a measurement is at present complicated even for simple model membranes composed of a single lipid and are prohibitively complicated for more biologically relevant multi-lipid systems. Indeed, the problem of measuring electrical parameters across a few nanometers in fluid is a complex one. Despite this complexity, the Gouy-Chapman theory, which assumes a nondiscrete surface charge density and treats the aqueous phase as a constant dielectric

medium, can be applied to lipid membranes to describe effective surface potentials at long range and can be further augmented by charge regulation mechanisms (Section 1.6 below) to accurately model experimental measurements of the lipid membrane surface potential [9].

1.4 Atomic Force Microscopy

The Atomic Force Microscope (AFM) [10], is a microscope with an imaging resolution which can approach fractions of a nanometer. It is a member of the family of instruments known as the scanning probe microscopes. They all operate by scanning a sharpened tip across the sample and obtaining surface information from the interaction between the sample and the surface. The AFM in particular, is able to operate in both fluid and has been of great utility in biology. In addition to imaging, the AFM is also able to measure forces with resolution approaching a few piconewtons. The AFM measures topography by raster scanning a very sharp tip along the surface being imaged.

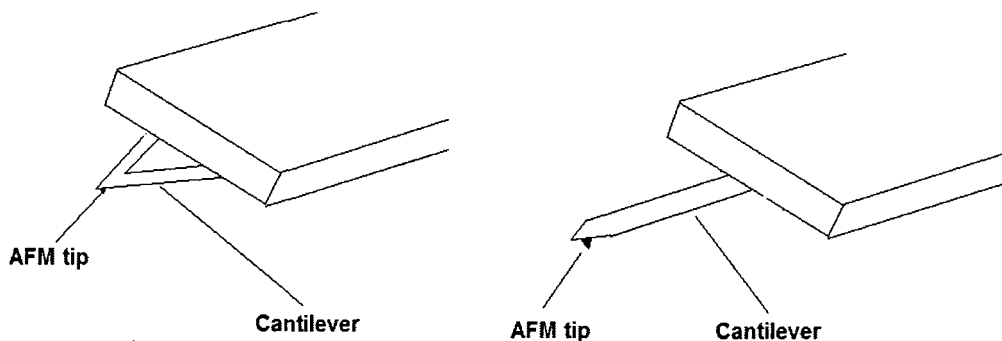


Figure 1.5: Schematic of typical AFM tip-cantilever assemblies.

The deviations in the tip position during scanning are measured and correlated with surface topography and a 3D image of the surface is reconstructed. The most commonly used AFM systems rely on a laser bounced off the AFM tip assembly onto a split photodiode to detect the variations in tip position (Figure 1.1), the commercial AFM used in our studies also employed this system. As the tip is scanned across the sample surface, the tip undergoes deformations which result in the laser beam spot being deflected. The split photodiode can detect the beam spot movement by differential signals from its different sections.

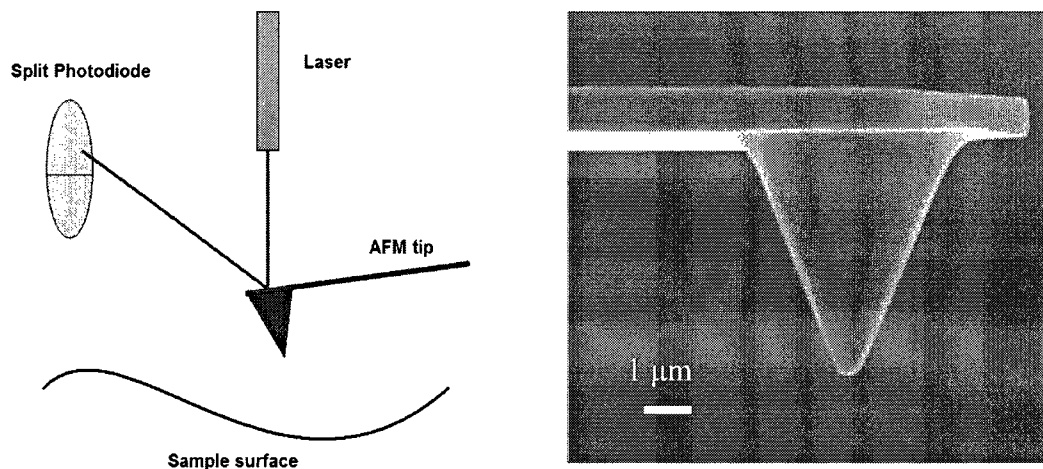


Figure 1.6: (Left) Schematic of an AFM optical detection system; a laser is bounced off the back of the AFM tip and directed to a split photodiode. (Right) Scanning Electron Microscope image of an AFM tip.

AFM is able to image in fluid and as a result, is able to image biological structures under near-native conditions. AFM has been used to image cells [11], DNA strands [12], antibodies [13] and many other biological structures.

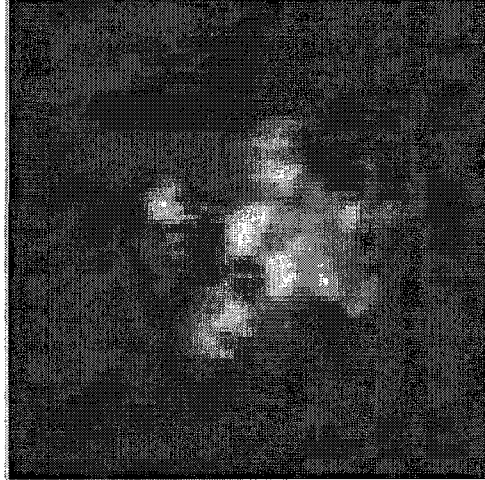


Figure 1.7: AFM image of an IgM antibody (image is approximately 20 nm x 20 nm in size). Image taken from Reference [13].

In addition to topography, AFM is also able to obtain qualitative information about the nature of the sample being imaged. For example, recent work has shown that AFM imaging can be used to differentiate between healthy and cancerous cells [14, 15].

As mentioned above, the AFM is able to measure force versus distance curves. These “force curves” are able to provide information about the properties of the tip, the sample, and the medium in between. Material properties such as elasticity, adhesion and surface charge density can be characterized using force curves. Thus, AFM force curve analysis has found applications in many fields including biology.

In an AFM force curve measurement the, tip-cantilever assembly is held stationary in the horizontal direction and is moved up and down vertically relative to the sample. The vertical position of the tip and deflection of the cantilever are recorded and converted to force-versus-distance curves (see Figure 1.8). The stochastic nature of force curves requires that many individual force curves be taken in order to obtain accurate physical information.

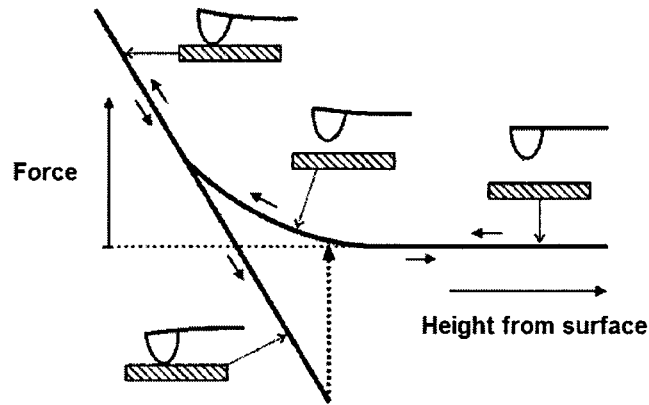


Figure 1.8: Schematic of a typical AFM force-distance curve showing both approach and retract curves. Image taken from Reference [16].

Force curves are used to characterize adhesion, chemical bond strength, electrostatic double layer forces and many other physical phenomena. More specific to this thesis, AFM force curves are used to characterize lipid membrane electrostatics.

1.5 Membrane electrostatics with AFM

Biomembranes are complex structures composed of many components. In addition to containing many different types of lipids, they also contain a number of other molecules such as membranes proteins. In order to make the study of membrane function tractable, model systems composed of a few lipids are typically used. For AFM studies of membrane electrostatics, supported lipid bilayers are used as model systems.

These are formed over smooth flat substrates such as glass or mica and are ideal for AFM studies. A number of methods for forming these supported bilayers exist. Of them, the

most convenient and reproducible method is to use vesicle fusion on to the substrate [17, 18]. Figure 1.9 is a schematic of the bilayer preparation process. We have used this method of vesicle preparation in our studies.

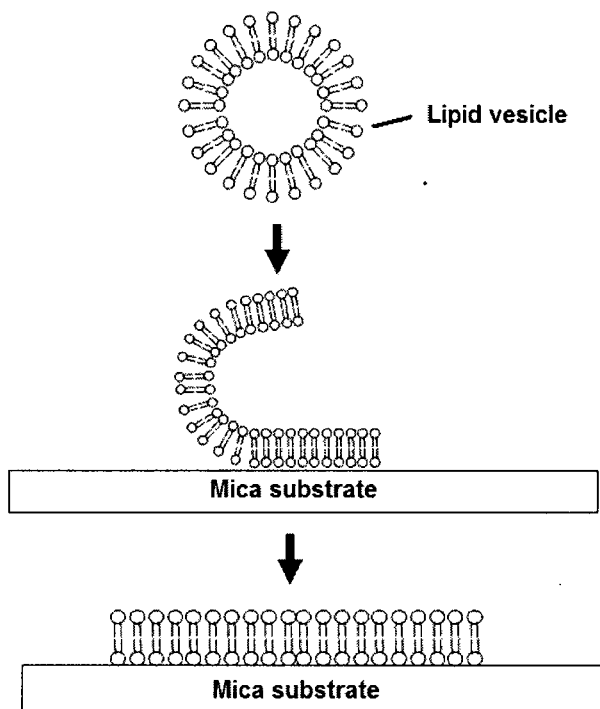


Figure 1.9: Schematic of supported lipid bilayer preparation by vesicle fusion. When preformed lipid vesicles are exposed to a flat substrate (mica in the above case), they rupture and form supported lipid bilayers.

Additionally, the existence of a water layer between the lower leaflet and the substrate has been proven for such supported lipid bilayers[19, 20]. This makes them a somewhat better approximation to a biomembrane.

1.6 Electrostatic double layer force and charge regulation

The electrostatic double-layer force arises because of surface charges at interfaces. Water in particular has a high dielectric constant. Thus, surface charges dissociation into the water is very common. The surface charge is balanced by dissolved counterions which are attracted back towards the surface by the electric field. These are not reabsorbed but, instead, form a diffuse cloud close to the surface. Taken together the ions and charged surface are known as the electric double layer. When another surface approaches, the double layer is perturbed, and the results in a force known as the double-layer force. When the approaching surface charges have the same sign, the concentration of ions between the surfaces always increases. This results in a repulsive force [21]. The electrostatic double-layer force can be calculated using continuum theory based on work by Gouy, Chapman, Debye, and Huckel for electric double layers.

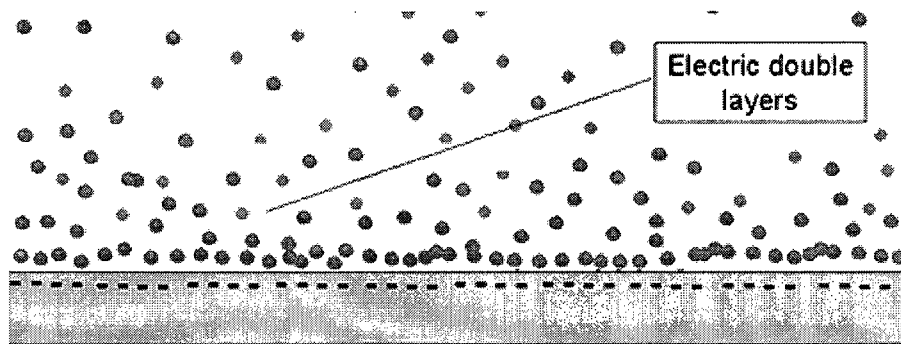


Figure 1.10: Schematic of the diffuse electric double layer formed over a negatively charged surface. The red dots represent positive counterions. The density of the counterions close to the surface is higher than in the bulk. This cloud of positive counterions is the diffuse electric double layer.

AFM tips made of silicon nitride are commonly used in studies of biological samples in fluid and we have used such tips in our work. The surface chemistry of silicon nitride is

well characterized [22, 23] and it is known that silicon nitride surfaces carry possess a net negative charge in water at physiological pH ($\text{pH} = 7$). Thus the electrostatic interaction between charged lipid surfaces and charged silicon nitride AFM tips is interpreted in terms of the electric double layer force. Theoretical considerations show that if two surfaces with constant surface charge density approach each in an electrolyte, the pressure and hence the double layer force between them approaches infinity [24].

In reality, when two such charged surfaces approach contact, the counterions are forced to readsorb onto their original surface sites. Thus, as their separation approaches zero the surface charge density also reduces, i.e., it becomes a function of surface separation. This is known as charge regulation. The effect of charge regulation is always to reduce the effective repulsion below that calculated on the assumption of constant surface charge[24].

1.7 Charge regulation at lipid interfaces

In lipids, the above mentioned form of charge regulation occurs when counterions bind to the headgroups of the lipids and form a stern layer which results in a reduction in the membrane surface charge density [25]. Another form of charge regulation that is unique to lipids also exists. Unlike most other surfaces, individual lipid molecules in bilayers, and hence the surface charges they carry, possess lateral mobility. Thus, lipids are able to rearrange themselves in response to the presence of an approaching charged surface so as to minimize the interaction energy. This phenomenon is known as mobile lipid charge regulation [26] and is thought to be important in biological macroion-lipid interactions.

Chapter 2

Quantitative Membrane Electrostatics with AFM

2.1 Introduction

This chapter presents an overview of the work done by others, on quantitative membrane electrostatics using AFM [1]. The work discussed herein forms the foundation for the original work done by us in Chapter 3. In Chapter 1, we have discussed the importance of membrane electrostatics. Many probes and techniques have been developed to measure the electrostatic potentials of lipid membranes. Of these, atomic force microscope (AFM) is a highly noninvasive probe. The AFM is able to image in fluid with nanometer-scale topographical resolution [27, 28]. With its ability to image in fluid, AFM is useful for biological applications because it can image biological structures under near-native conditions. The AFM can also hold the tip over a specified position and measure force as a function of tip-sample separation. This force-curve analysis has been applied to molecular recognition interactions [29-32], protein unfolding [33], and nonspecific hydrophobic, hydration, van der Waals, and electrostatic interactions [34, 35]. At low electrolyte concentrations (0.5–5 mM) and tip-sample separations greater than a few nanometers, one can reach a regime where electrostatics dominates the long-range tip sample interaction.

The electric double layer force between a spherical tip and planar sample in electrolyte solution was derived [24] starting from the formula for the pressure between two charged planes in an electrolyte solution [36]. Accordingly, the force F is given by

$$F = \frac{4\pi R \lambda \sigma_{tip} \sigma_{sample}}{\epsilon_{electrolyte} \epsilon_o} e^{-\frac{D}{\lambda}} \quad (2.1)$$

where R is the tip radius, λ is the Debye screening length, σ_{tip} and σ_{sample} are the tip and sample charge densities, and D is the tip-sample separation [36]. This equation was derived using several assumptions, including small surface potentials, tip-sample separations larger than the Debye length, and tip radii larger than the separation, $R \gg D \gg \lambda$. In spite of these approximations, this expression has been successfully used to describe experimental measurements in terms of the force dependence on tip-sample separation, tip radius, electrolyte concentration, and pH [35, 37-43]. It has been widely applied to electrostatic interactions between Si_3N_4 (silicon nitride) probe tips and inorganic surfaces, as well as lipid membranes [42-47]. Another method of analyzing AFM force data is to numerically simulate the tip-sample force by solving the full nonlinear Poisson-Boltzmann equation with proper boundary conditions [36, 48-51]. To get membrane surface electrostatic information, one can interpret the experimental data with Equation 2.1 or with a numerical simulation. To make a quantitative measurement using an analytical approach, one must measure all the constant parameters in Equation 2.1. If one uses a numerical approach, the proper boundary conditions must be chosen. To test the quantitative surface charge density measurement method for biomembrane analysis, we have measured force curves over supported lipid membranes of zwitterionic

PC with increasing mole fractions of anionic PS (X_{ps}) to increase the surface charge density and potential in a predictable way. Electrostatic measurements were made in buffer with different tips, on membranes with X_{ps} varying from 0.05 to 0.5.

2.2 Materials and methods

2.2.1 Preparation of DOPC:DOPS supported lipid membranes

Following the general methods described in [1], Lyophilized dioleoylphosphatidylserine (DOPS-anionic lipid) and dioleoylphosphatidylcholine (DOPC-zwitterionic lipid) obtained from Avanti Polar Lipids, Alabaster, AL, were dissolved in chloroform and mixed at various relative mole fractions. The mixtures were dried under nitrogen gas, placed under low vacuum for at least 1 h, and then hydrated with deoxygenated double deionized water for a final lipid concentration of ~ 2 mg/mL. The lipid solutions stood overnight in a dark, room-temperature environment followed by vigorous agitation for at least 1 h. The resulting multilamellar vesicle solutions were refrigerated and stored for up to two weeks. Supported lipid bilayer membranes for AFM analysis were formed on mica substrates by vesicle fusion [17]. A 100 mL drop of the multilamellar vesicle solution at a lipid concentration of 20–200 mg/mL (diluted from stock in double deionized water) was placed on the mica for 20 min at 35–40 °C. The sample was then rinsed with double deionized water and placed under a 0.5 mM solution of Tris buffer at pH 7 for AFM imaging and analysis in fluid tapping mode (Multimode NanoScope IV, Veeco Metrology, Santa Barbara, CA).

2.2.2 Force curve acquisition and analysis

All AFM experiments were carried out with silicon nitride probes (DNP, cantilever C, Veeco Probes). Both tip and sample were immersed in 0.5 mM Tris buffer (pH 7) throughout the experiment. To record force curves over lipids, the AFM tip was situated over a lipid membrane by first imaging the topography and then positioning the tip over the lipid region. For reference measurements, force curves were recorded over the silicon nitride chip of a probe from the same wafer as the tip. The gold coating on this chip was first etched with aqua regia to reduce interference from the reflected AFM laser beam. Force curves were recorded with the Nanoscope software (version 5.30r1) with 10,240 data points over an 800 nm scan range at 1.4 Hz, with tip retraction triggered for a maximum cantilever deflection corresponding to 5 nN. The raw force curves (cantilever deflection voltage on the y axis versus z piezo position on the x axis) were exported and read into MatLab where they were converted to force versus tip-sample separation, D , by the following methods which are similar to those described previously [1, 38, 47]:

1. A y-axis offset was applied to set the deflection voltage equal to zero for large tip-sample separation.
2. An interference intensity function was fit to the large tip-sample separation region and the resulting function was subtracted from the entire force curve to compensate for optical interference between reflections from the cantilever and the sample surface.

3. A line was fit to the contact region of the force curve to determine the cantilever deflection sensitivity, s , so that the curve could be converted from tip deflection voltage to relative tip deflection position in nm.
4. The cantilever deflection was subtracted from the sample z position to convert the force curve to a plot of tip deflection versus tip-sample separation, D , rather than sample position.
5. The point of zero tip-sample separation was defined as the intersection of the lines that fit the large tip-sample separation and the contact region of the force curve.
6. The cantilever deflections were converted to forces with the measured spring constant.
7. Hundreds of such force curves were averaged before carrying out the electrostatic analysis described below.

2.2.3 Tip charge density measurement

Following the strategy described in previous works [1, 49], Silicon Nitride tips were taken from a wafer (DNP, Veeco Probes), which provided silicon nitride reference surfaces with an identical preparation, stoichiometry, and history as the tip. Force curves were recorded over the identical silicon nitride reference surface and used to find the surface charge density of the tip by the detailed analysis described below and summarized in Figure 2.3.

2.2.4 Tip radius and spring constant measurement

The radius of each individual AFM tip was measured from scanning electron microscope (SEM) images using the iterative method described in the literature [1]. The spring constant of each tip was directly measured by the added mass method [52]. The thermal resonance frequency of the cantilever was measured before and after the addition of a known mass, M , by micromanipulation, yielding frequencies ν_1 and ν_2 , respectively. The known mass was a 6 mm spherical silica bead with a well-defined shape and density (Bangs Laboratories, Fishers, IN). The shift in resonant frequency yields the spring constant using the following relation:

$$k = (2\pi)^2 \frac{M_1}{\left(\frac{1}{\nu_2^2}\right) - \left(\frac{1}{\nu_1^2}\right)} \quad (2.3)$$

2.2.5 Finite Element Modeling

Force curves were analyzed with numerical solutions to the full nonlinear Poisson-Boltzmann equation using a commercial software package (FlexPDE 5.0.8, PDE Solutions, Antioch, CA). To simulate the interaction between a silicon nitride AFM tip and a supported lipid membrane, the domains displayed in Figure 2.1 were set up.

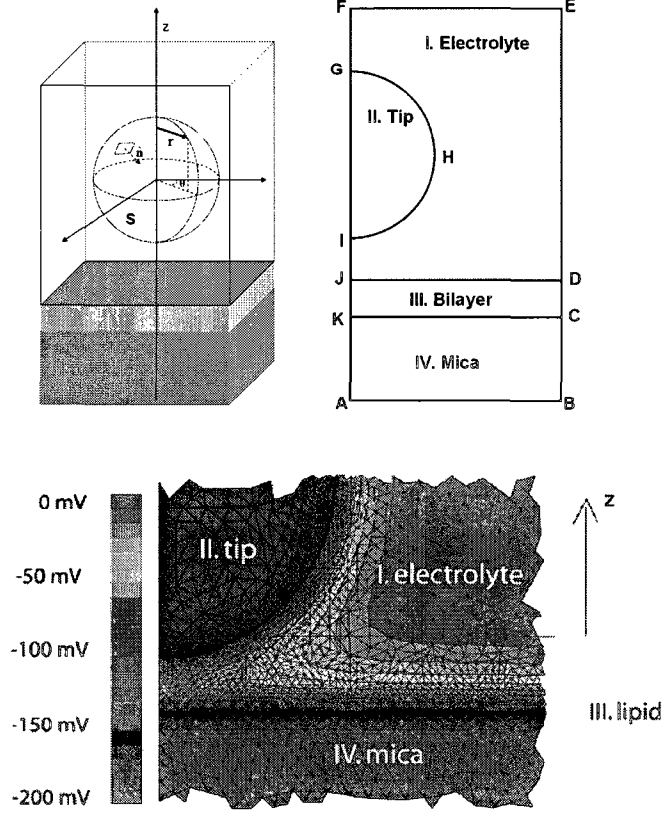


Figure 2.1: (Top Left) 3D schematic diagram, (Top Right) Finite Element Domains I to IV, not to scale. (Bottom) Portion of the mesh generated while solution is computed.

In Figure 2.1, Domain I corresponds to the aqueous phase between the tip and membrane.

The Poisson-Boltzmann equation in this domain was defined as

$$\nabla^2 \psi = \frac{2n_0 e}{\epsilon_{electrolyte} \epsilon_0} \sinh\left(\frac{e \psi}{k_B T}\right) \quad (2.4)$$

with electrostatic potential ψ , 1:1 monovalent electrolyte ion density n_0 , electron charge e , Boltzmann constant k_B , and dielectric constant $\epsilon_{electrolyte} = 79$. Domain II represents the

silicon nitride tip ($\varepsilon = 7$), Domain III the 5 nm thick lipid bilayer membrane ($\varepsilon = 2$), and Domain IV the mica substrate ($\varepsilon = 6$). Since there are no free charges in domain II, III and IV, the electrostatics potential in these domains are governed by the Laplace equation

$$\nabla^2 \psi = 0 \quad (2.5)$$

On line ABCDEF, the zero charge density boundary condition was applied:

$$\nabla \psi \cdot \mathbf{n} = 0 \quad (2.6)$$

Over line FGIJKA, radial symmetry holds as

$$\frac{\partial \psi}{\partial r} = 0 \quad (2.7)$$

Constant charge density boundary conditions (Neumann's condition) were applied [48] at the surface of the AFM tip (GHI) and at the upper surface of the lipid membrane (line JD):

$$\varepsilon_1 \nabla^{(1)} \psi \cdot \mathbf{n} - \varepsilon_2 \nabla^{(2)} \psi \cdot \mathbf{n} = -\sigma / \varepsilon_0 \quad (2.8)$$

where \mathbf{n} represents the vector normal to the surface in the direction pointing to the electrolyte solution. At the interface between the membrane and mica (line CK), continuity holds. To simulate the force curves between the silicon nitride AFM tip and the flat silicon nitride substrate, regions III and IV were merged into one layer and set to $\varepsilon = 7$. FlexPDE employs a modified Newton-Raphson iteration procedure to solve the nonlinear equations. An initial rough mesh was generated at the beginning of the simulation and an adaptive mesh algorithm iterated via a mesh refinement procedure until a tolerance of 10^{-5} was achieved. A portion of the refined mesh and the resulting electrostatic potentials are plotted in Figure 2.1 (bottom). The electrostatic potential and the electric field were evaluated at the tip-electrolyte boundary and exported for force calculations. Rotation of the tip curve $r(z)$ by 2π around the z -axis generates the closed

surface S (Figure 2.1, Top). Thus, the total force applied on the tip is given as the surface integral

$$\mathbf{F} = \int_S \mathbf{T} \cdot \hat{\mathbf{n}} dS \quad (2.9)$$

where \mathbf{n} is a unit normal vector pointing into the surface S ,

$$\hat{\mathbf{n}} = \frac{r'(z)\hat{\mathbf{z}} - \hat{\mathbf{r}}}{\sqrt{1 + r'^2}} \quad (2.10)$$

in which r is the tip curvature given as

$$r = \sqrt{\text{radius}^2 - z^2} \quad (2.11)$$

\mathbf{T} is the total stress tensor [50, 53]:

$$\mathbf{T} = (\Pi + \frac{1}{2} \epsilon \epsilon_0 \mathbf{E} \cdot \mathbf{E}) \mathbf{I} - \epsilon \epsilon_0 \mathbf{E} \mathbf{E} \quad (2.12)$$

in which Π is the osmotic pressure term

$$\Pi = 2n_0 k_B T (\cosh(e\psi/k_B T) - 1) \quad (2.13)$$

\mathbf{I} is the unit dyadic, \mathbf{E} is local electric field vector. The tip-sample force measured by the AFM can be described as the z component of Equation 2.9.

$$F_z = \int_{z_1}^{z_2} \left(r' \left[\Pi + \frac{1}{2} \epsilon \epsilon_0 E^2 - \epsilon \epsilon_0 E E_z \right] + \epsilon \epsilon_0 E E_r \right) 2\pi r dz \quad (2.14)$$

Equation 2.14 was numerically calculated based on the electrostatic field values and potentials exported from the simulation. Z_1 and Z_2 are the z -axis limits of the sphere. By changing the tip-sample separation, force curves were simulated. These curves were compared to the silicon nitride reference data, and σ_{tip} and σ_{sample} were adjusted to achieve a good match (Figure 2.3). Once the tip charge density was known, the same procedure was carried out on the lipid data to determine the long-range fit.

2.3 Results and discussion

Fits to Equation 2.1 yield the lipid surface charge density σ_{sample} , as a function of X_{ps} as shown in Figure 2.2. The error bars reflect contributions from the uncertainty in each parameter.

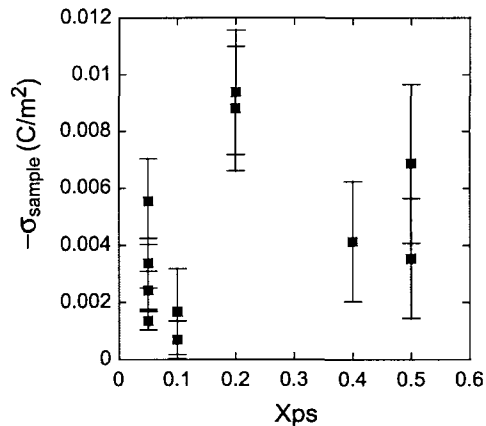


Figure 2.2: The lipid membrane charge densities determined by applying Equation 2.1 to the experimental force curves. The data do not follow the expected trend with DOPS mole fraction.

The use of Equation 2.1 in interpreting the data gives a result that shows no discernable trend, and the variation cannot be accounted for by the error. This is not entirely unexpected, considering the approximations that go into the derivation of Equation 2.1. In our measurements, the tip radii are significantly larger than the Debye length. In addition, the values of D that must be fit, approach λ at short range and exceed R at long range. Also, the surface potentials greatly exceed the range where the linearized Poisson-Boltzmann equation is applicable. Note that the negative result of Figure 2.2 does not necessarily mean that the functional dependences in Equation 2.1 are inaccurate. Several experiments have confirmed that Equation 2.1 accurately predicts the force dependence

on D , R , λ , and pH, but usually by only varying one parameter [35, 37-43, 54]. Also, the analytical model significantly underestimates the magnitude of the sample charge density. Thus, in order to circumvent the restrictive assumptions used in deriving Equation 2.1, the experimental data was interpreted by solving the full PB equation with a Finite Element numerical simulation of the AFM lipid system [1]. The tip radius and spring constants were measured and the tip-sample force was obtained by solving the nonlinear Poisson-Boltzmann equation under normal boundary conditions [36, 48-51]- which is in this case equivalent to surface charge density of the lipid. The boundary condition was adjusted in the simulation and fit with the averaged force curve data. The best fit of the simulation to the experimental data was interpreted as the surface charge density of the lipid as shown in the Figure 2.3.

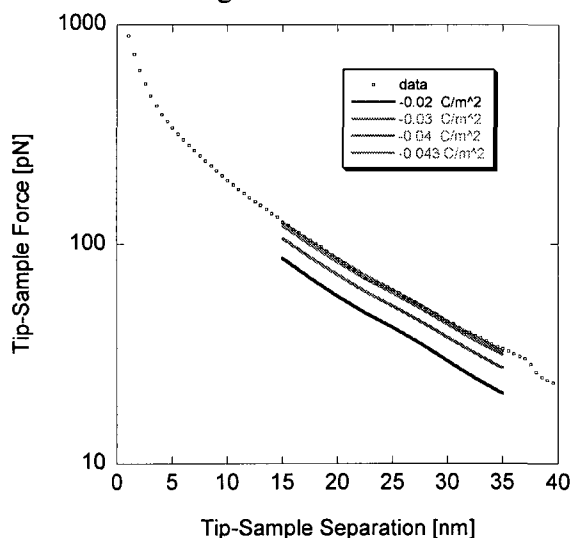


Figure 2.3: Comparing data and simulation results. Each solid, colored line represents the computationally simulated force curve obtained by using various guesses as to the lipid surface charge density. Note that the data is fit to the model only in the long-range region (1–4 Debye lengths).

The analysis was carried out by manually adjusting σ_{sample} in force-curve simulations and comparing it to experimentally measured force curves in the long-range region (1–4 Debye lengths). In Figure 2.3, the best fit of simulation to data is for the charge density -0.043 C/m^2 , which is interpreted as the membrane surface charge density. The reference silicon nitride data were used to characterize σ_{tip} in a similar manner to that used in the analytical procedure.

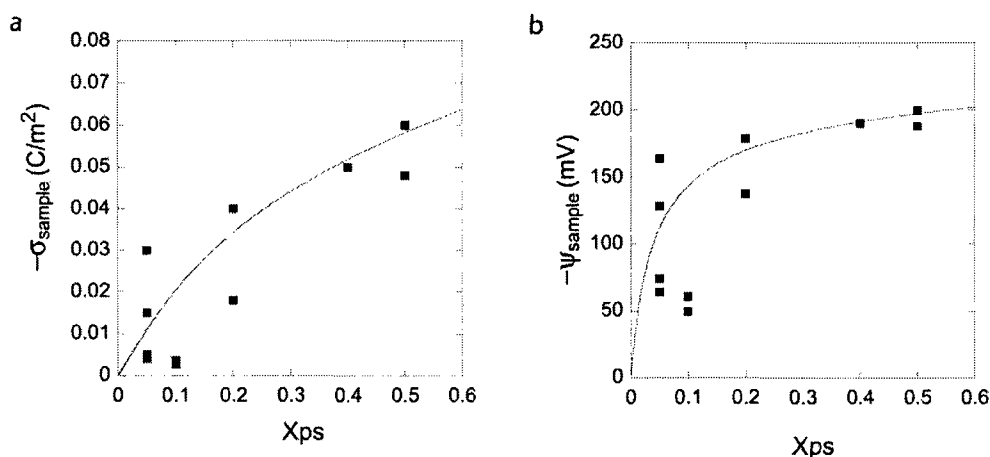


Figure 2.4: (a) Lipid membrane charge densities and, (b) surface potentials determined by a numerical analysis of the experimental force curves. The data (squares) follow the curves predicted by the Gouy-Chapman-Stern model (line).

Unlike the result obtained with Equation 2.1, the numerical data follow the trend displayed in Figure 2.4. The numerical results shown in Figure 2.4 are in quantitative agreement with a simple Gouy-Chapman-Stern (GCS) model of the membrane, which accounts for charge regulation [25]. In the model, electrolyte cations can bind to the PS headgroups to form a Stern layer that neutralizes their contribution to the effective surface charge density. The cation binding is described by a Langmuir isotherm and the effect of the surface potential on the cation surface concentration is taken into account. The model therefore has only three input parameters: the bulk electrolyte concentration

(C_o), the area per lipid (A), and the binding constant of the electrolyte cation to the PS headgroup (K). Note that the solid line in Figure 2.4 is not a fit, but rather the result of this model for $C_o = 0.47$ mM, $A = 0.7$ nm², and $K = 1$ M⁻¹ [9]. In the numerical simulations, charge regulation was not included in the boundary condition [25] since a simple constant field boundary condition was applied evenly to the entire sample surface. This method of analysis is not exact since the presence of the tip locally alters the surface potential, thus requiring a boundary condition that allows a spatially varying surface field. In addition, two other charge regulation mechanisms were not considered. The effect of the surface potential on protonation of the PS headgroup was not included since the pK of the headgroup is 2, very much lower than the pH of the buffer [55]. More significantly, not included was a charge regulation mechanism specific to lipid membranes that takes into account the high level of mobility of the charged lipids [26]. Unlike an inorganic surface, charged headgroups in a fluid lipid membrane can move and redistribute in response to a potential. Calculations of this effect find that it can be significant for cases such as DNA bound to a cationic membrane. Chapter 3 will show that the constant charge density boundary condition model described in this chapter deviates divergently from the data in the short-range (< 1 Debye length) regime and that mobile lipid charge regulation needs to be accounted for in order to characterize this observed short-range deviation.

Chapter 3

Mobile Lipid Charge Regulation in Membranes

3.1 Introduction

Biomembranes are usually in a fluid state in which individual membrane components are free to move in lateral directions within the plane of the membrane, whereas their vertical movements are highly restricted. Since the lipids are mobile, the membrane can respond to interacting macromolecules by locally changing its composition. For example, consider the adsorption of a negatively charged DNA molecule onto a membrane containing a fraction of cationic lipids initially randomly dispersed among nonionic lipids. Upon adsorption, mobile lipid charge regulation is thought to occur, resulting in cationic lipids diffusing towards the interaction zone and neutral lipids diffusing away, thereby minimizing the electrostatic interaction free energy. DNA-cationic lipid complexes have been observed experimentally [56, 57] and are candidates for nonviral gene-therapy and for vehicles to transport DNA into cells [58-62]. These types of systems have been studied extensively [63-66]. In particular, it has been shown that spatial inhomogeneities in the membrane surface-charge density, in response to interactions with the DNA, can have a significant effect on the phase behavior and stability of DNA-cationic lipid complexes [67]. In addition, numerous other recent theoretical studies on the adsorption of charged macromolecules other than DNA can be found in the literature [68-70]. Recently, Netz et. al. [26, 71] have extended the Poisson-Boltzmann theory of membrane electrostatics to include mobile lipid charge regulation and have applied it to

single DNA strand-lipid membrane interactions. They have suggested that a membrane composed of mobile surface groups will differ appreciably in its interaction with DNA, when compared with a membrane having immobile surface charges. Experimental evidence for lipid mobility resulting from macromolecule-lipid interactions has been in the form of lipid phase separation observations. These have been reported for various systems; e.g., the binding of polylysine [72], cardiotoxin II [73], cytochrome c [74] and model peptides [75] onto monovalently charged membranes, as well as membranes containing multivalent lipids [76, 77]. This evidence has typically been at the micron-scale, observed using fluorescence optical microscopy.

The following work represents the first experimental demonstration of mobile lipid charge regulation at the nanoscale using AFM. We will show that short-range deviation of the AFM data from the model given in Chapter 2 is due to mobile lipid charge regulation under the influence of the AFM tip (Figure 3.1).

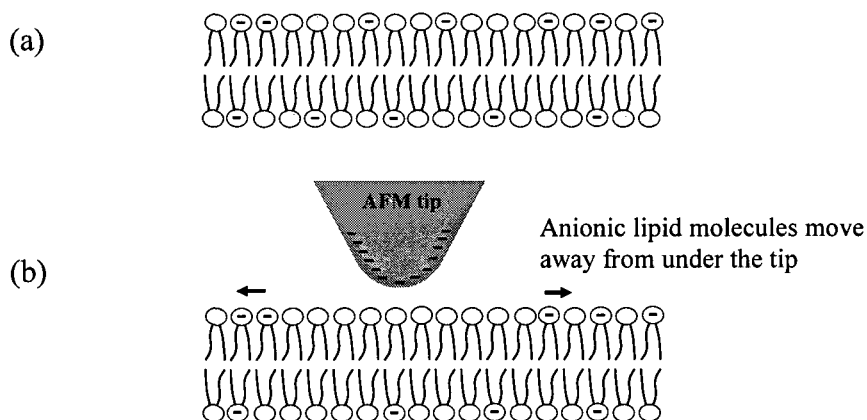


Figure 3.1: Schematic of AFM tip-induced mobile charge regulation. Neutral lipids are shown in yellow and the anionic lipids are shown in white. (a) In an unperturbed lipid bilayer, the neutral and the anionic lipids are distributed homogeneously. (b) The close proximity of the negatively charged AFM tip induces the negative lipid molecules to move away and results in a patch of mostly neutral lipids forming underneath the AFM tip.

As shown in Figure 3.2, the results obtained from the model given in Chapter 2 start deviating from the AFM data at short tip-sample separations (11 nm and less in the figure below).

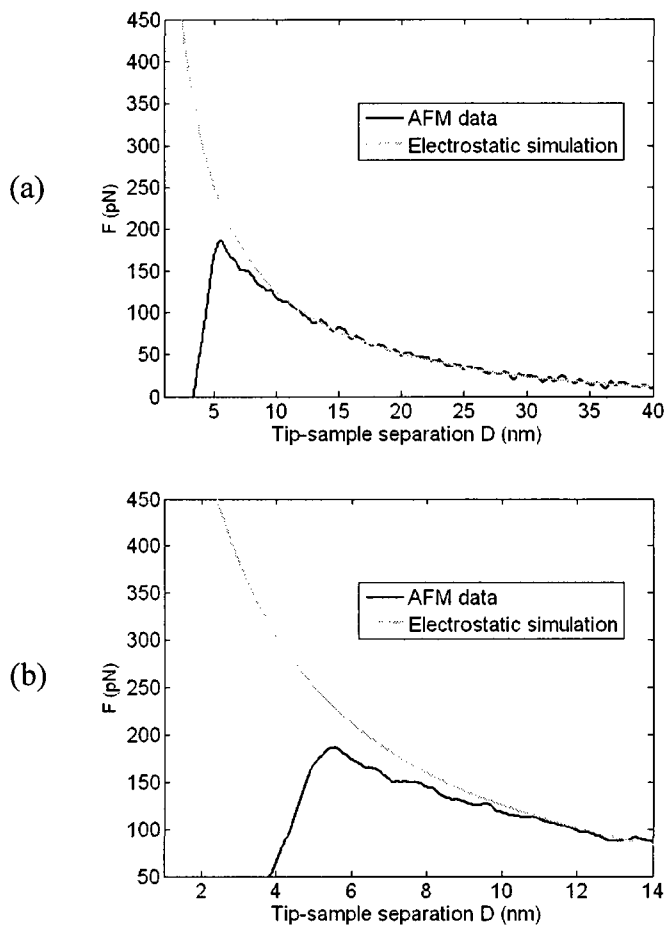


Figure 3.2: (a) The fixed charged density model is a good fit for the data for $D > 11$ nm. (b) A closer view of the same data shown in (a) reveals that the simulation deviates from the data when $D < 11$ nm. The data is for a 1:5, DOPC:DOPS mixture.

The fixed surface charge density model of Chapter 2 consistently over-estimates the force in the short-range. Thus, we reason that the short-range correction must be due to a lessening in repulsion between the tip and the lipid. We will first show that the van der Waals interaction between the tip and the sample does not account for the observed short ranged deviation. Next, we will demonstrate that the AFM tip-induced counterion

binding onto the lipid is also insufficient to account for the short range deviation. As a control, we will show that for silicon nitride, which contains immobile surface charges, short range deviations can be accounted for using an AFM tip-induced counterion binding charge regulation model. Finally, we will show that a mobile lipid charge regulation model explains the behavior of the AFM data over lipids, in the short-range. Furthermore, force curves over immobile gel-phase lipids are shown not to exhibit the short-range deviations seen in highly mobile fluid-phase lipids.

3.2 Experimental method

3.2.1 Preparation of DOPC:DOPS supported lipid membranes

Following the general methods described in [1], Lyophilized dioleoylphosphatidylserine (DOPS-anionic lipid) and dioleoylphosphatidylcholine (DOPC-zwitterionic lipid) obtained from Avanti Polar Lipids, Alabaster, AL, were dissolved in chloroform and mixed at various relative mole fractions. The mixtures were dried under nitrogen gas, placed under low vacuum for at least 1 h, and then hydrated with deoxygenated double deionized water for a final lipid concentration of ~2 mg/mL. The lipid solutions stood overnight in a dark, room-temperature environment followed by vigorous agitation for at least 1 h. The resulting multilamellar vesicle solutions were refrigerated and stored for up to two weeks. Supported lipid bilayer membranes for AFM analysis were formed on mica substrates by vesicle fusion [17]. A 100 μ L drop of the multilamellar vesicle solution at a lipid concentration of 20–200 mg/mL (diluted from stock in double deionized water) was placed on the mica for 20 min at 35–40 °C. The sample was then rinsed with double

deionized water and placed under a 0.5 mM solution of Tris buffer at pH 7 for AFM imaging and analysis in fluid tapping mode (Multimode NanoScope IV, Veeco Metrology, Santa Barbara, CA).

3.2.2 Preparation of DOPC:DOPS:DMPC:DMPS supported lipid membranes

Lyophilized dioleoylphosphatidylserine (DOPS-anionic), dimyristoylphosphatidylserine (DMPS-anionic), dioleoylphosphatidylcholine (DOPC-zwitterionic) and dimyristoylphosphatidylcholine (DMPC-zwitterionic) obtained from Avanti Polar Lipids, Alabaster, AL, were dissolved in chloroform and mixed at mole fractions of 1:3 and 1:3 respectively and then these components were also mixed together. The mixture was dried under nitrogen gas, placed under low vacuum for at least 1.5 h, and then hydrated with deoxygenated deionized water for a final lipid concentration of ~2 mg/mL. The lipid solutions were heated to 50 °C and agitated for 30 minutes and stood overnight in a dark, room-temperature environment followed by vigorous agitation for at least 1 h. The resulting multilamellar vesicle solutions were refrigerated and stored for up to two weeks. Supported lipid bilayer membranes for AFM analysis were formed on mica substrates by vesicle fusion. A multilamellar vesicle solution at a lipid concentration of 20–200 mg/mL (diluted from stock in deionized water) was heated to 50 °C and a 100 mL drop was placed on the mica for 20 min at 35–40 °C. The sample was then rinsed with double deionized water and placed under a 0.5 mM solution of Tris buffer at pH 7 for AFM imaging and analysis in fluid tapping mode (Multimode NanoScope IV, Veeco Metrology, Santa Barbara, CA).

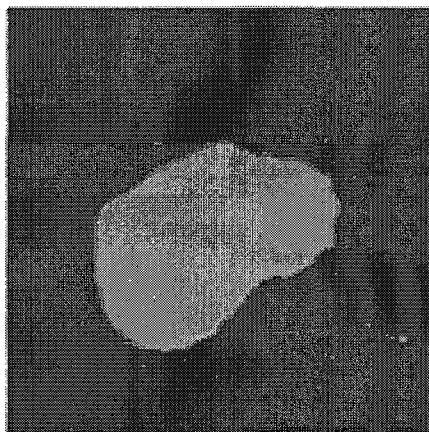


Figure 3.3: Fluid AFM topographical image of a 1:9, DMPC:DMPS lipid patch. We are able to identify the lipid bilayer patch from its cross-sectional height which is 5 nm. The scan size is 1x1 μm .

3.2.3 Computational analysis

Van der Waals forces between the tip and the sample were calculated using a custom-written MatLab routine. Tip-induced charge regulation was modeled as follows. We first created a finite element simulation domain of the tip and the lipid sample using the general methods described in Section 2.2 of this thesis. We then visually chose the D value, which we will call D_0 , at which the Chapter 2 model starts deviating significantly from the data. For the sample data in Figure 3.2, $D_0 = 11$ nm (see Figure 3.5). For D_0 and lower, we include the tip-induced perturbations of the lipid surface into our finite element calculation in the form of a variable surface charge density boundary condition (see Figure 3.4).

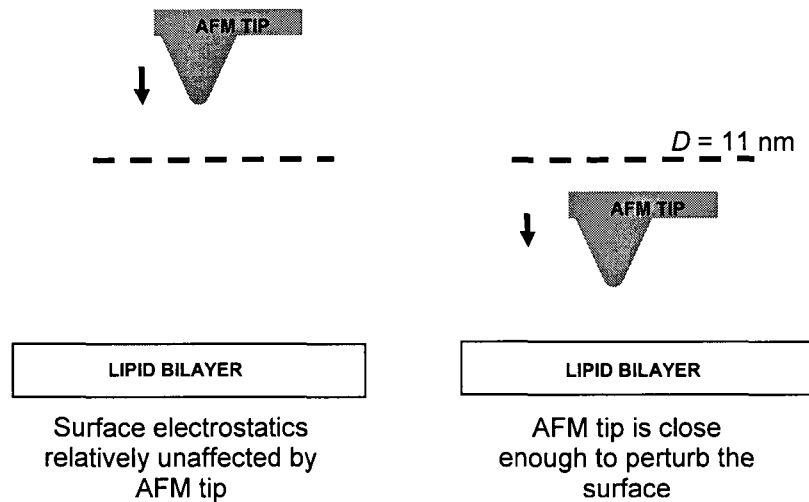


Figure 3.4: (Left) The finite element model is solved with a constant charge density boundary condition from $D = 40 \text{ nm}$ to $D = 11 \text{ nm}$ as in Chapter 2. Note that these values of D are for the data shown in Figure 3.2. For other data sets, the D values will be different. For $D = 11 \text{ nm}$ and less, we vary the lipids surface charge density according to the law governing the phenomenon being addressed (i.e. whether it is counterion binding or mobile lipid charge regulation).

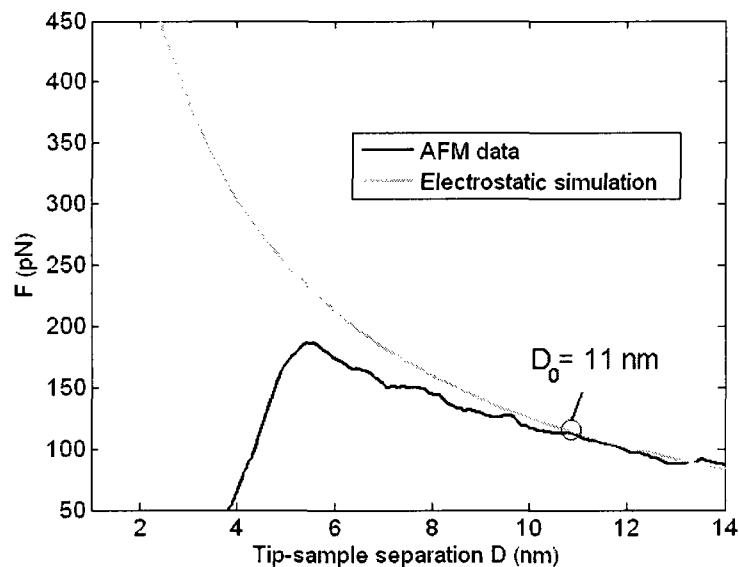
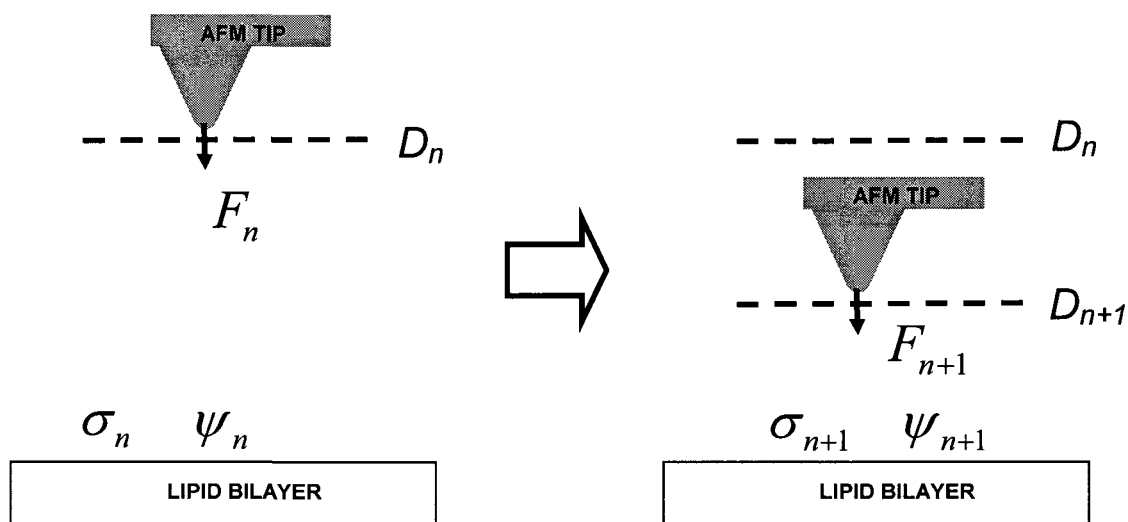


Figure 3.5: D_0 is chosen as the point where the AFM data starts deviating significantly from the electrostatic simulation of Chapter 2. For the above sample, $D_0 = 11 \text{ nm}$. The AFM data and the electrostatic simulation shown here is the same as in Figure 3.2.

The variable surface charge density was included in the simulation as follows. With the tip at D_0 , we ran the simulation using the surface charge density obtained from applying the method described in Chapter 2, this is the unperturbed surface charge density σ_0 . We then set the tip at D_1 , ($D_1 = D_0 - 0.5$ nm) and set the surface charge density to σ_1 . Here, σ_1 was calculated as a function of the lipid surface potential underneath the tip ψ_0 , when the tip was at D_0 . We ran the simulation with D_1 , σ_1 and then repeated the same procedure for $D_2, D_3, \dots, D_n, D_{n+1}$ as shown in the schematic in Figure 3.6, with $D_{n+1} = D_n - 0.5$ nm



$$\sigma_{n+1} = g(\psi_n)$$

Figure 3.6: Schematic of how the tip-induced charge regulation finite element model is implemented. Here, ψ is the surface potential, σ is the surface charge density of the lipid bilayer and F is the electrostatic force on the tip. The functional form of g will depend on the form of charge regulation being considered (e.g. charge regulation due to counterion binding).

3.3 Results

3.3.1 Van der Waals interaction

The model given in Chapter 2 makes several assumptions regarding the behavior of the lipid surface. In particular, it does not account for the perturbations of the lipid surface due to the presence of the AFM tip. While neglecting the effect of the AFM tip might be valid at longer distances, at shorter distances, the presence of the charged tip may have an effect on the lipid surface potential. In addition, the previous model does not account for van der Waals attractions.

For a sphere-plane geometry, the van der Waals force (F) is given by [16, 78-80]

$$F = \frac{A_H R}{6X^2} \quad (3.1)$$

Where X is the distance between the surfaces, R is the radius of the sphere and A_H is the Hamaker constant [81]. We have used the sphere-plane approximation thus far and continue to do so in this calculation. We use the experimentally measured value of the AFM tip radius as R . The value of the Hamaker constant was calculated to be 2×10^{-20} J [82, 83]. In doing the above calculations, we assume that the electric double layer forces and the van der Waals forces are independent and can be added [26].

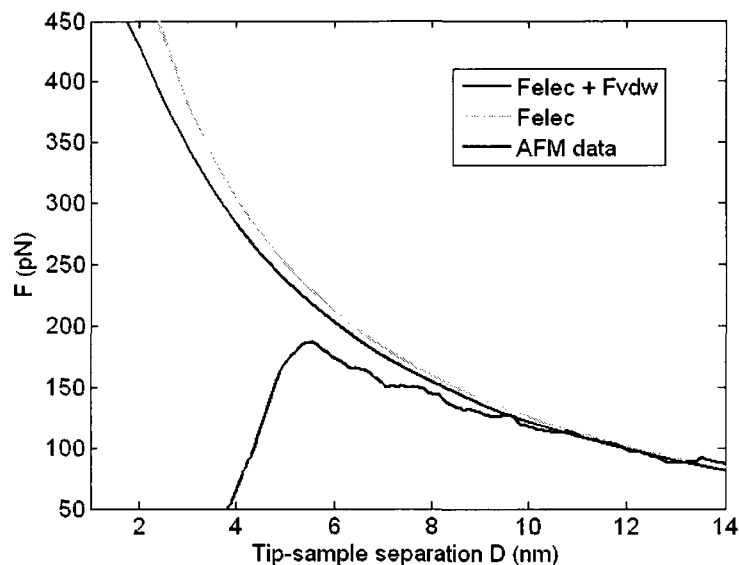


Figure 3.7: Comparison of the AFM data with the van der Waals computational model. The AFM data and the electrostatic simulation shown here are the same as in Figure 3.2.

As seen in Figure 3.7, the inclusion of the van der Waal attraction does not account for the discrepancy in the previous model. Even when unrealistically large values of A_H were used (several orders of magnitude larger than the actual A_H) we were not able to see a fit to the experimental data.

3.3.2 Charge regulation due to counterion binding; lipids vs. silicon nitride

In the Gouy-Chapman-Stern (GCS) theory of lipid membrane electrostatics, a source of charge regulation is the binding of counter ions onto the charged headgroups of the lipids. In applying the GCS model to our system, electrolyte cations bind to the PS headgroups to form a Stern layer. The cation binding is described by a Langmuir isotherm and the effect of the surface potential on the cation surface concentration is taken into account.

The stern layer formed by cation binding is included in the simulation using the following. The charge density for a mixed PC/PS membrane, σ_0 , is given by X_{PS} , the mole fraction of PS, and A , the membrane area per lipid.

$$\sigma_0 = \frac{X_{ps}e}{A} \quad (3.2)$$

Electrolyte cations bind to form a Stern layer on the PS head groups resulting in a reduced surface charge density. Assuming that this follows a Langmuir isotherm, the charge density due to the remaining charged lipids is,

$$\sigma = \frac{\sigma_0}{(1 + KC)} \quad (3.3)$$

where C is the molar concentration of the cation, and K is its association constant to the lipid headgroup. Since the surface potential alters the surface cation concentration according to the Boltzmann relation,

$$\sigma = \frac{\sigma_0}{1 + KC_0 \exp\left[-\frac{e\psi}{k_B T}\right]} \quad (3.4)$$

where C_0 is the bulk molar concentration of the electrolyte and ψ is the surface potential. Since the Chapter 2 model does not apply charge regulation due to cation binding onto the lipids, the charge density calculated from that models long-range fit is σ_0 . Based on Equation 3.4, we use the following iterative formula for the charge density in each step of our calculation

$$\sigma_{n+1} = \frac{\sigma_n}{1 + KC_0 \exp\left[-\frac{e\psi_n}{k_B T}\right]} \quad (3.5)$$

Here, ψ_n is the potential on the surface of the lipid, vertically below the apex of the tip. We take the potential just below the tip because the force signal is largely determined by the membrane region directly below the tip with variations in the potential elsewhere

having little effect. Analyses of the numerical simulations revealed that the difference in membrane surface potential between points directly below the tip and off to the side where the tip had no effect was only 2% [1]. The association constant for cation binding to the PS headgroup is $K = 1 \text{ M}^{-1}$ [84] and $C_0 = 0.5 \text{ mM}$ is the known bulk electrolyte concentration. We ran the finite element simulation with this cation binding model. Here, the simulation was run at a separation of 11 nm to get the far values. Next, the tip was brought closer, and the surface charge was adjusted based on the previous step's surface potential, in this case it was adjusted according to the Langmuir Isotherm (see Section 3.2.3). The simulation was run with this new surface charge and the force was calculated. However, as shown in Figure 3.8 below, cation binding based charge regulation was insufficient to fit the experimental data.

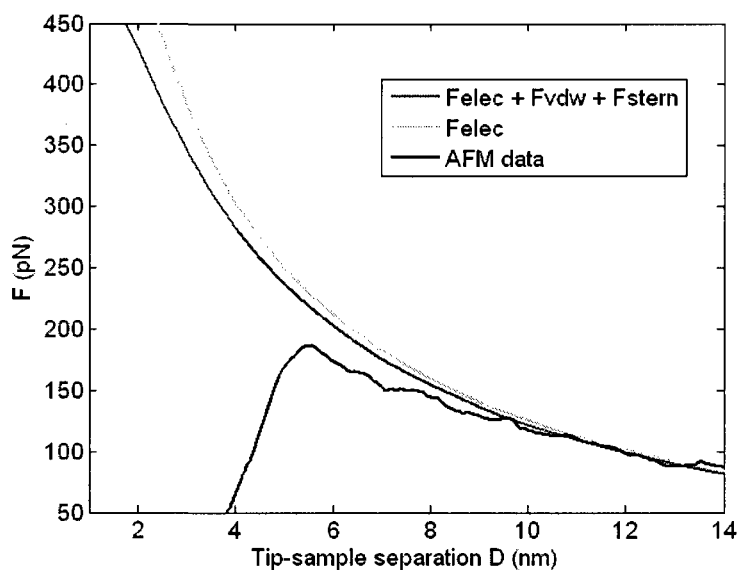


Figure 3.8: Comparison of the AFM data with the van der Waals and stern layer inclusive computational model. The AFM data and the electrostatic simulation shown here is the same as in Figure 3.2.

Another charge regulation mechanism is protonation of the PS headgroup. The pK of that group is < 2 and since our pH is much larger, we can ignore this as a possible cause of the short range variation [1, 55]. As a control, we have shown below that counterion binding alone is sufficiently strong to account for short range variations from the constant surface charge model in the case of a surface with immobile charge groups, specifically, a silicon nitride surface. In contrast to the mobile lipid charges, silicon nitride is an example of an inorganic surface which has immobile discrete charges. When force curves taken over silicon nitride surfaces are fit using the constant surface charge density model, we see the same type of long-range fit and short range deviation as seen in the lipid bilayer data. We use Equation 3.5 with association constant $K = 10^{-7} \text{ M}^{-1}$ [23] and consider counterion binding to the Si_3N_4 surface in our simulation. In contrast to the lipid case, we see an effect on the short range fit when the cation binding is included. Figure 3.9 shows such a fit to a Si_3N_4 sample.

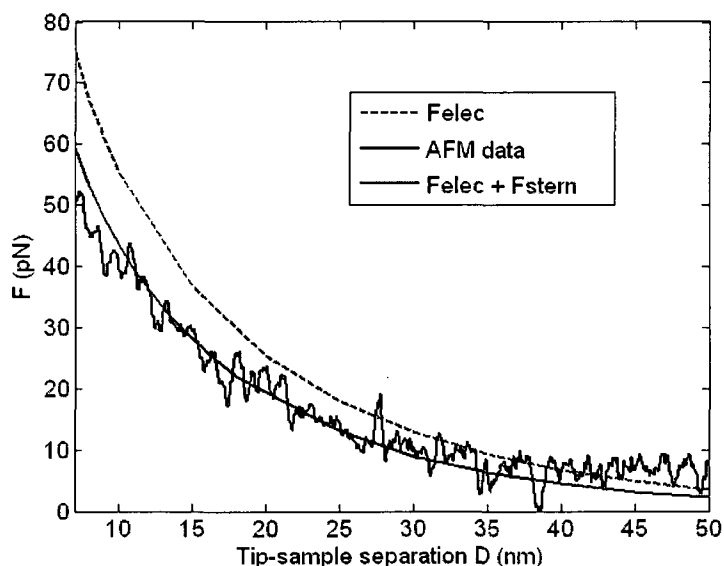


Figure 3.9: AFM data for a Si_3N_4 sample fit with a model that includes charge regulation due to cation binding via a Langmuir isotherm. (Black, solid curve) - AFM data, (Red, dashed curve) - constant surface charge electrostatic model, (Blue, solid curve) - cation binding model.

As can be seen in Figure 3.9, the counterion binding model produces a better fit to the experimental data for the silicon nitride when compared with the fit produced by the counterion binding model applied to the lipid case in Figure 3.8. This is not unexpected since the analysis in Chapter 2 produced a fit to the GCS model in spite of that analysis not explicitly accounting for the stern layers presence, suggesting that the stern layer has little affect in the case of these particular experiments. This could be due to the large differences in the association constants between the lipid and the silicon nitride surfaces.

3.3.3 Mobile lipid charge regulation

Another charge regulation mechanism is that due to the lateral mobility of the individual lipids. Unlike most inorganic surfaces, the individual lipids and hence the charges in the bilayer are highly mobile. This mobility has been found to be significant for cases such as DNA binding to cationic lipids. Attempts have been made to include this mobility into the GCS model of lipid electrostatics [26, 71, 85, 86]. Here, we will show that the negatively charged silicon nitride AFM tip induces mobile lipid charge regulation in a manner akin to that which is thought to occur when a charged macro-molecule such as DNA or protein interacts with a charged lipid bilayer. We modeled the mobile lipid charge regulation using a Boltzmann relaxation formula (Equation 3.6).

$$\sigma_{n+1} = \sigma_n \exp\left[\frac{e}{k_B T}(\psi_n - \psi_\infty)\right] \quad (3.6)$$

Here ψ_∞ is the unperturbed surface potential which is obtained from the simulation when the tip is set very far away (200 nm) from the lipid surface. Using the same method as for Equation 3.5, we modeled mobile lipid charge regulation using the above Boltzmann relaxation equation. As shown in Figure 3.10, our mobile lipid charge regulation model gives a good fit for the short range AFM data.

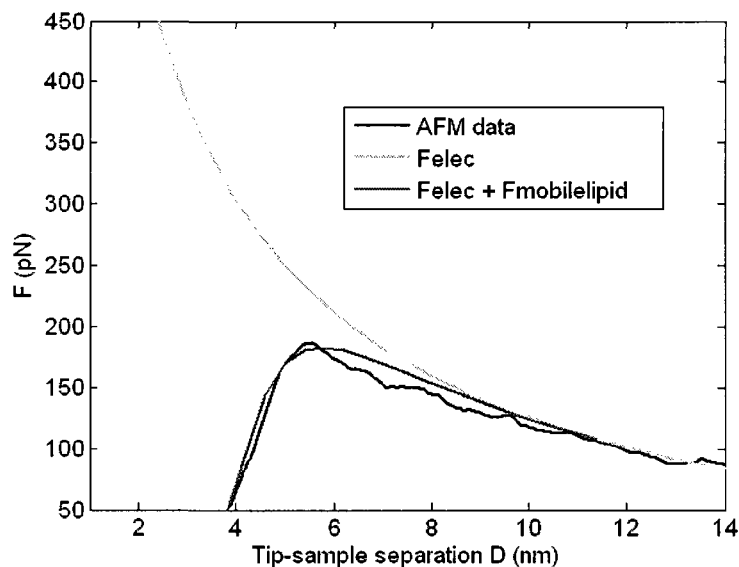


Figure 3.10: Data fit with the Boltzmann relaxation model of mobile lipid charge regulation. The AFM data and the electrostatic simulation shown here is the same as in Figure 3.2.

To make sure that lipid motion would result in a physically reasonable number of lipids moving out within the time scale of our experiment, we did the following calculation. Consider the 2-D Brownian motion that would occur in the top leaflet of the bilayer in the absence of any velocity fields. The mean square displacement of an individual lipid molecule would then be given by

$$\langle r^2 \rangle = 4D_l t \quad (3.7)$$

Where D_l is the lateral diffusion constant of the lipid and t is the time. The AFM tip speed is 2240 nm/s. In our mobile lipid model, we calculate our modified force values in steps of 0.5 nm. At the above speed, it takes approximately 250 μ s to move that distance. Using Equation 3.7, and taking $D_l = 4.2 \times 10^{-12}$ m²/s for DOPC [87], we find that the root mean square displacement is approximately 100 nm. The force on the AFM is mostly influenced by the region of lipid under the tip. Given that the AFM tip is also on the order of 100 nm, the lipid motion is of a time scale and length scale accessible to the AFM. Furthermore, the minimum change in surface charge density seen in the between steps of our simulation is also on the order of a few tens of individual lipid charges. Thus, in terms of the lateral mobility of the lipids and the AFM's ability to detect them, our mobile lipid simulation is physically reasonable.

3.3.4 Comparing mobile lipid charge regulation on gel and fluid phase lipids

As a further demonstration of the importance of mobile lipid charge regulation in the analysis of lipid-AFM force curve data, we have harnessed the large mobility differences between gel and fluid phase lipid species. The individual molecules of a lipid in gel phase are quite rigid and stationary in comparison to those of the fluid phase lipid. If we consider structurally similar (i.e. having the same tail groups) gel and fluid lipid patches of similar surface charge density, tip induced mobile lipid charge regulation would be more prominent over fluid phase lipid patches. Thus, the force curves over fluid patches

would show short range deviations as before. In comparison, the force curve profiles over gel phase lipid patch would not show such short range deviations.

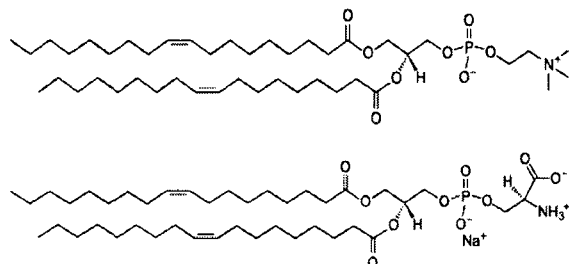


Figure 3.11: (Top) DOPC-neutral at pH 7, (Bottom) DOPS-anionic. A mixture of these lipids will be in fluid phase at room temperature.

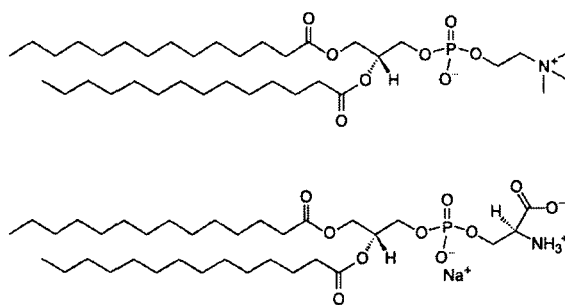


Figure 3.12: (Top) DMPC-neutral at pH 7, (Bottom) DMPS-anionic. A mixture of these lipids will be in fluid phase at room temperature.

Following section 3.2.2, we prepared a 4-lipid component mixture composed of DOPC, DOPS, DMPC and DMPS. The DOPC:DOPS and DMPC:DMPS mixtures were of identical molar ratios (both having 1:3, PS:PC) so that the lipid patches would have very similar surface charge densities. The supported lipid bilayer made of the DMPC:DMPS mixture has a gel-fluid transition temperature of 36 °C and forms gel phase patches at room temperature [88]. The DOPC:DOPS mixture forms fluid phase lipid.

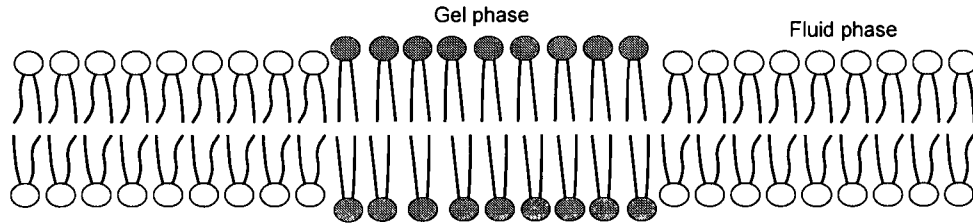


Figure 3.13: Schematic of gel phase (blue) and fluid phase (yellow) lipid bilayers coexisting. The gel phase lipid regions are more rigidly packed and are thicker than the loosely packed fluid phase lipid regions

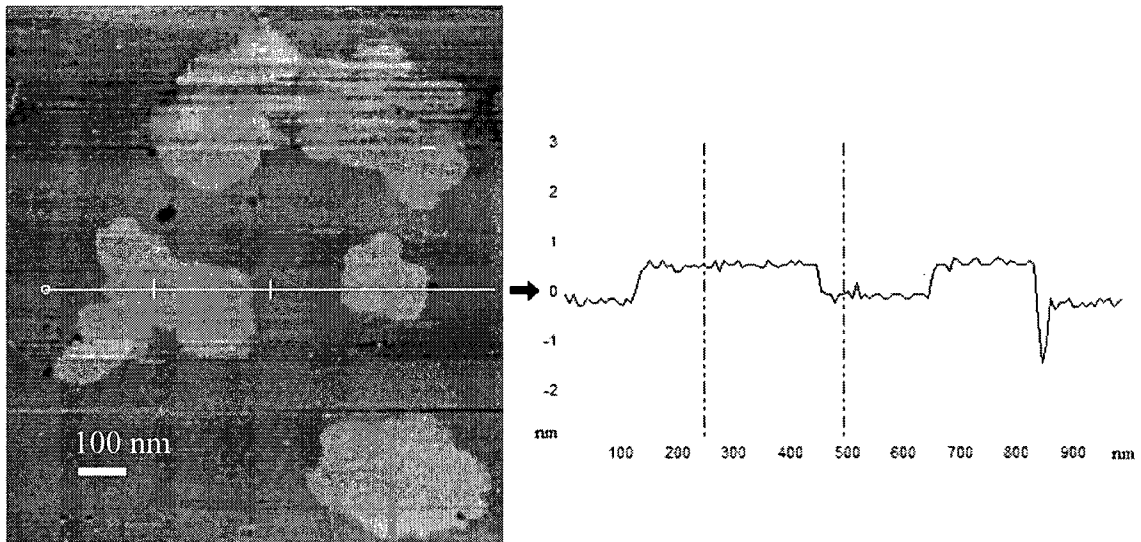


Figure 3.14: AFM imaging data of the DOPC:DOPS:DMPC:DMPS mixture. (Left) Topography of the lipid mix, the lighter colors represent taller features – the image is 1x1 μm in size. (Right) A cross section taken through the topographical image – as shown by the white line. The height difference between the lighter and the darker areas is 0.8 nm, identifying the lighter regions as gel phase patches residing in a sea of fluid phase lipid sea.

In Figure 3.14, the topographical data clearly shows lighter areas which are 0.8 nm taller than the surrounding lipid. These are identifiable as the gel phase lipid patches of DMPC:DMPS located in a sea of fluid phase DOPC:DOPS. In order to compare the lipid mobility based charge regulation of the gel and fluid lipids, we needed to have the surface

charge densities of both the gel phase and the fluid phase be equal. We used Fluid Electric Force Microscopy (FEFM) [45] to compare surface charge densities of the two phases. FEFM involves the AFM scanning the sample topography, lifting the tip to a predetermined lift height and rescanning the along the same contour, at the lift height (see Figure 3.15). For flat samples, the force on the tip during the lift scan is directly proportional to the samples surface charge density. Thus using FEFM we get a simultaneous topography and charge contrast map.

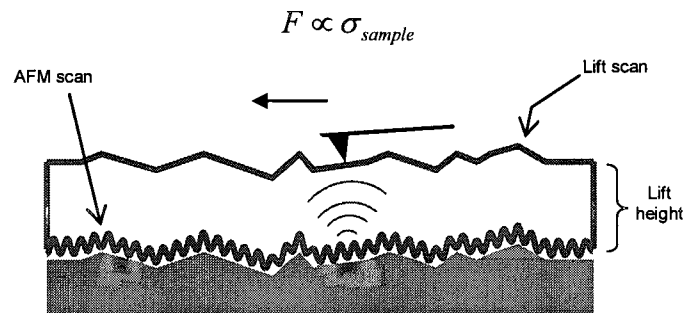


Figure 3.15: Schematic of Fluid Electric Force Microscopy (FEFM). The force F experienced by the tip during the lift scan is directly proportional to the samples surface charge density σ_{sample} .

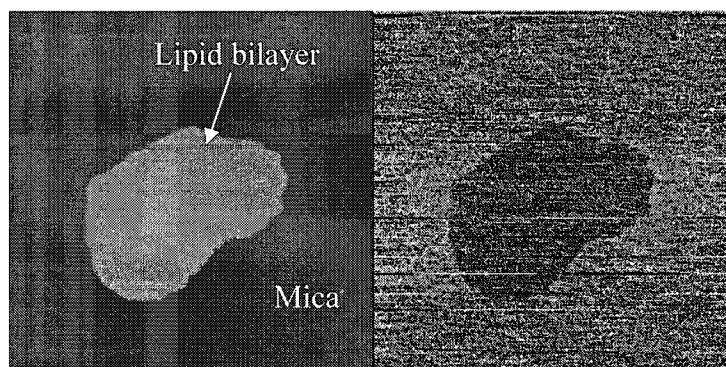


Figure 3.16: AFM topography image of a 1:9, DMPC:DMPS lipid patch. (Left) Topographic image of the lipid bilayer. (Right) Charge map of the same area showing the charge contrast between the lipid and the mica. The scan size is $1 \times 1 \mu\text{m}$.

Figure 3.16 is an example of a FEFM image with significant charge contrast, in this case between mica and an anionic lipid patch.

We prepared 4-lipid gel/fluid mixtures and performed FEFM scans of them. Figure 3.17 shows such a sample. As can be seen in the right panel of Figure 3.17, we do not find discernable charge contrast between the gel and the fluid phase areas.

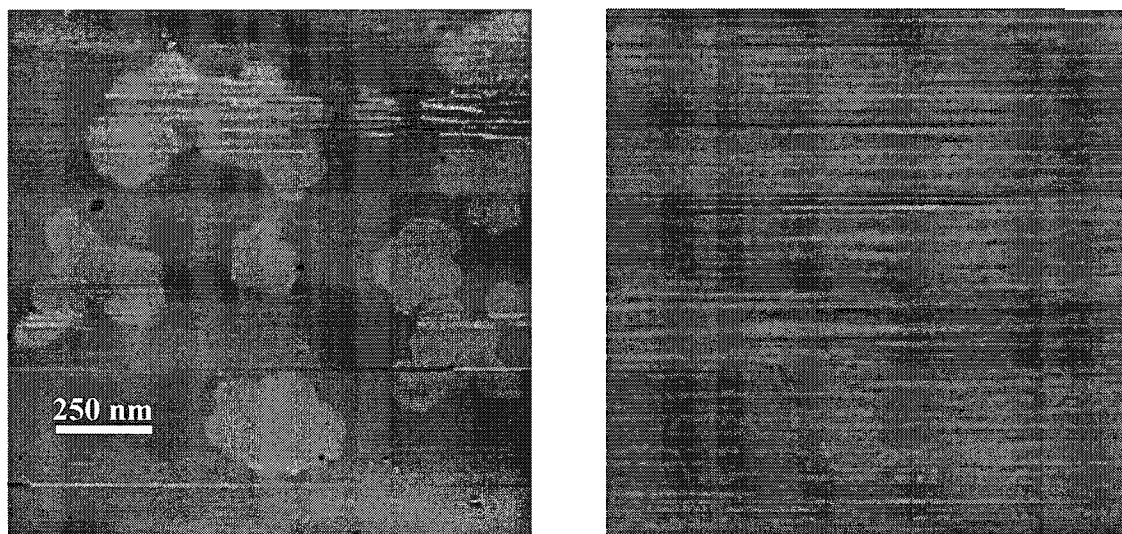


Figure 3.17: FEFM imaging of the DOPC:DOPS:DMPC:DMPS mixture. (Left) Topography of the lipid mix, the lighter colors represent taller features. (Right) The charge map of the same region showing no discernable charge contrast. The scan size is $2 \times 2 \mu\text{m}$.

Once a sample that had gel and fluid patches of equal charge density, as measured by FEFM, was obtained, force curves were recorded over both the gel phase lipid patches and also on adjacent fluid phase regions following the method described in Section 2.2 of this thesis. By taking force curves in the same region, in the same experiment, we are able to interpret any variations in the gel and fluid force curves in terms of the relative mobility of each phase and are also able to minimize any effects caused by variability in AFM tips and electrolyte concentrations. The raw force curve data was processed using the methods described in Section 2.2 and converted into force as shown in Figures 3.18.

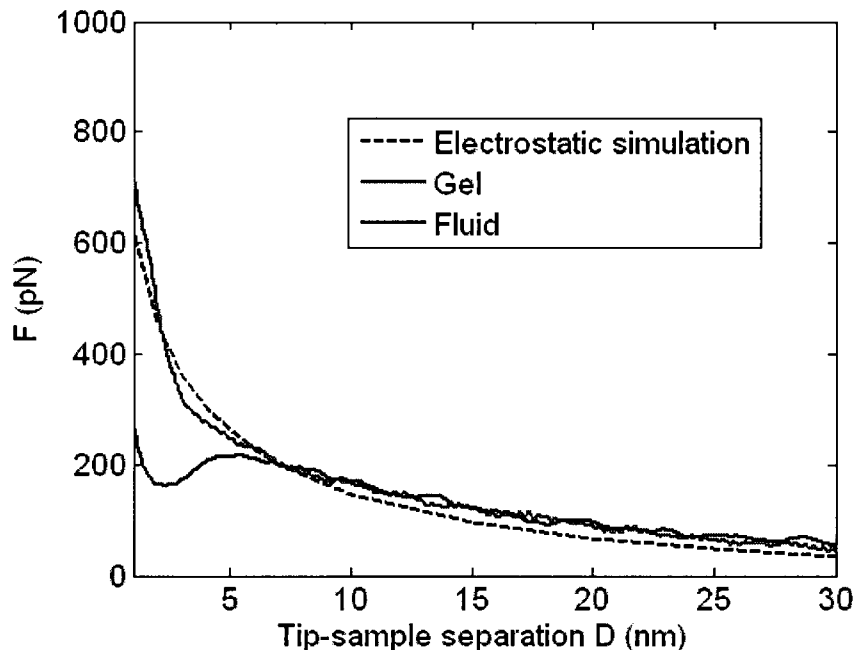


Figure 3.18: Comparison of force curves taken over fluid phase (Blue curve) and gel phase (Red curve) shown with a constant surface charge electrostatic fit (Black dashed curve). Both sets of data were taken with the same tip during the same experiment and the electrostatic fit was obtained for a surface charge density of -0.04 C/m^2 .

In Figure 3.18, the force over the fluid phase (shown in blue) is lower than that over the gel phase (shown in blue), at tip separations less than 7 nm. This, in addition to the previous data, suggests that the tip induced mobile lipid charge regulation is more

prominent over the fluid phase as opposed to gel phase. When the tip is further than 7 nm from the surface, we see an overlap of the two force curves. This is due to the equality in surface charge of the two phases when the tip is far away and not perturbing the surface. Figure 3.18 also shows the gel and fluid data compared with a theoretical force curve obtained using the model in Chapter 2. The gel phase force data follows the same general shape as the theoretical model due to immobility of the lipids and weak counterion binding. The fluid phase shows the short range deviation from the model when the tip is closer than 7 nm from the surface. As shown in this study, this is due to tip induced mobile lipid charge regulation.

3.4 Discussion

We have used a combination of finite element computer simulations and experimental AFM data to show that mobile charge regulation accounts for the short range (< 1 Debye length) electrostatic force over anionic lipids measured by AFM in a low salt solution. We have accounted for van der Waal interactions and cation binding based charge regulation in our calculations and found the mobility of the lipid to be the dominant factor in characterizing the short range AFM electrostatic force data over lipids. Control experiments on silicon nitride surfaces, whose surface charges are immobile, showed that the short ranged AFM force data could be adequately accounted for by the formation of a stern layer due to cation binding. In contrast, a stern layer was insufficient to account for the short-range force seen over fluid phase lipids. The strongest evidence for tip-induced

mobile lipid charge regulation was presented in the form of clear differences in the short range behavior of mobile, fluid phase lipids when compared to immobile gel phase lipids, in the presence of the AFM tip. The contrasting behavior of the mobile vs. immobile surfaces observed in our experiments is also in good qualitative agreement with theoretical predictions made by others (Figure 3.19) [26].

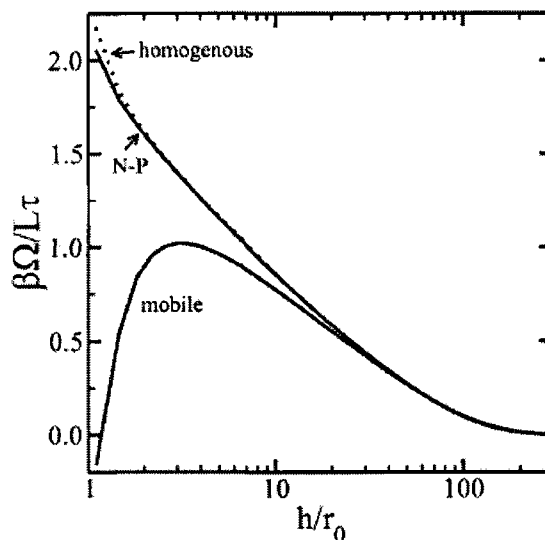


Figure 3.19: From Reference [26]. Theoretical prediction of a DNA–membrane interaction for three different models of a membrane. The DNA was modeled as a charged cylinder of length L and radius r_0 . $\beta\Omega$ is the grand potential and τ is the line charge density and h is the distance from lipid surface to center of cylinder. In the above, the quantity plotted on the y-axis is electrostatic interaction energy between the cylinder and the surface and the quantity plotted on the x-axis is related to the DNA-membrane separation. (*mobile*): the model membrane is composed of three types of mobile surface groups: negatively charged, neutral and dissociable. (*N-P*): membrane charges result from dissociation as in case I, but surface ions are immobile. (*homogeneous*): charges are fixed, surface ions are immobile. In all three cases, the homogeneous surface charge density far away from the DNA is equal and corresponds to an effective homogeneous charge density of $\rho_c = -1/4.8 \text{ nm}^2$ ($\kappa^{-1} = 50 \text{ nm}$).

As with our data, the above figure shows long-range overlap and short-range deviations in the mobile versus immobile theoretical surface charge models.

We computationally implemented the mobile lipid regulation with a model based on a Boltzmann relaxation. The model resulted in an excellent short-range fit. While the

goodness of the fit to the experimental data was somewhat dependent on the step size, $D_{n+1} - D_n$, we used in our iteration procedure (Section 3.2.3). However, the general direction of the fit was independent of step size. We analyzed the accuracy of our finite element model using a resolution test whereby we increased the mesh density by many orders of magnitude corresponding to an increase in the output tolerance from 10^{-5} to 10^{-8} . This type of a test is commonly used as a measure of the accuracy of a finite element model. The results were found to be independent of mesh density and are thus convergent. Possible reasons for the step size dependence could be that the solutions of the partial differential equation might be very sensitive to variations in initial conditions and that such small changes might be propagating divergently with each step. More detailed work will take into account such factors. Aside from that it is important to note that this is the first attempt at interpreting AFM data by considering mobile lipid charge regulation. The use of a continuum model in representing discrete structures and the use of a Boltzmann relaxation to represent individual lipid motions is not ideal. However, since the AFM tip is much larger than the individual lipid molecules, this approximation is reasonable. In our analysis, we have varied the surface charge density of the entire lipid surface at each iteration. Ideally, we would require a boundary condition that allows a spatially varying surface charge. But, having multiple boundary conditions adds an additional degree of complexity to the simulation and could be prone to propagation of errors. In addition, the force signal is largely determined by the membrane region directly below the tip, with variations in the potential elsewhere having little effect.

We have shown that mobile lipid charge regulation can be used to characterize short range deviations from the expected electrostatics, over lipid surfaces. Recent theoretical

work has shown that this type of charge regulation plays an important role in biological macroion-lipid interactions, especially in protein-lipid, peptide-lipid and DNA-lipid interactions [72-77]. In particular, DNA-cationic lipid complexes have shown potential for therapeutic applications such as transporting DNA into cells and non-viral gene therapy [58-62]. Our analysis offers a means of gaining further understanding of this important phenomenon at the nanometer scale.

References

1. Yang, Y., K.M. Mayer, and J.H. Hafner, *Quantitative membrane electrostatics with the atomic force microscope*. Biophysical Journal, 2007. **92**(6): p. 1966-1974.
2. Cevc, G., *Membrane Electrostatics*. Biochimica Et Biophysica Acta, 1990. **1031**(3): p. 311-382.
3. MacKinnon, R., *Voltage sensor meets lipid membrane*. Science, 2004. **306**(5700): p. 1304-1305.
4. McLaughlin, S. and D. Murray, *Plasma membrane phosphoinositide organization by protein electrostatics*. Nature, 2005. **438**(7068): p. 605-611.
5. Clarke, R.J., *The dipole potential of phospholipid membranes and methods for its detection*. Advances in Colloid and Interface Science, 2001. **89**: p. 263-281.
6. Voglino, L., T.J. McIntosh, and S.A. Simon, *Modulation of the binding of signal peptides to lipid bilayers by dipoles near the hydrocarbon-water interface*. Biochemistry, 1998. **37**(35): p. 12241-12252.
7. Cladera, J. and P. O'Shea, *Intramembrane molecular dipoles affect the membrane insertion and folding of a model amphiphilic peptide*. Biophysical Journal, 1998. **74**(5): p. 2434-2442.
8. Cafiso, D.S., *Dipole potentials and spontaneous curvature: membrane properties that could mediate anesthesia*. Toxicology Letters, 1998. **101**: p. 431-439.
9. Winiski, A.P., et al., *An Experimental Test of the Discreteness-of-Charge Effect in Positive and Negative Lipid Bilayers*. Biochemistry, 1986. **25**(25): p. 8206-8214.

10. Binnig, G., C.F. Quate, and C. Gerber, *Atomic Force Microscope*. Physical Review Letters, 1986. **56**(9): p. 930.
11. Tetard, L., et al., *Imaging nanoparticles in cells by nanomechanical holography*. Nature Nanotechnology, 2008. **3**(8): p. 501-505.
12. Lyubchenko, Y., et al., *Atomic Force Microscopy of Long DNA - Imaging in Air and under Water*. Proceedings of the National Academy of Sciences of the United States of America, 1993. **90**(6): p. 2137-2140.
13. Hafner, J.H., C.L. Cheung, and C.M. Lieber, *Growth of nanotubes for probe microscopy tips*. Nature, 1999. **398**(6730): p. 761.
14. Cross, S.E., et al., *Nanomechanical analysis of cells from cancer patients*. Nature Nanotechnology, 2007. **2**(12): p. 780-783.
15. Cross, S.E., et al., *AFM-based analysis of human metastatic cancer cells*. Nature Nanotechnology, 2008. **19**(38): p. -.
16. Butt, H.J., B. Cappella, and M. Kappl, *Force measurements with the atomic force microscope: Technique, interpretation and applications*. Surface Science Reports, 2005. **59**(1-6): p. 1-152.
17. Brian, A.A. and H.M. McConnell, *Allogeneic Stimulation of Cyto-Toxic T-Cells by Supported Planar Membranes*. Proceedings of the National Academy of Sciences of the United States of America-Biological Sciences, 1984. **81**(19): p. 6159-6163.
18. McConnell, H.M., et al., *Supported Planar Membranes in Studies of Cell-Cell Recognition in the Immune-System*. Biochimica Et Biophysica Acta, 1986. **864**(1): p. 95-106.

19. Koenig, B.W., et al., *Neutron reflectivity and atomic force microscopy studies of a lipid bilayer in water adsorbed to the surface of a silicon single crystal*. *Langmuir*, 1996. **12**(5): p. 1343-1350.
20. Bayerl, T.M. and M. Bloom, *Physical-Properties of Single Phospholipid-Bilayers Adsorbed to Micro Glass-Beads - a New Vesicular Model System Studied by H-2-Nuclear Magnetic-Resonance*. *Biophysical Journal*, 1990. **58**(2): p. 357-362.
21. Chan, D.Y.C. and D.J. Mitchell, *The Free-Energy of an Electrical Double-Layer*. *Journal of Colloid and Interface Science*, 1983. **95**(1): p. 193-197.
22. Zhmud, B.V., J. Sonnefeld, and L. Bergstrom, *Influence of chemical pretreatment on the surface properties of silicon nitride powder*. *Colloids and Surfaces a-Physicochemical and Engineering Aspects*, 1999. **158**(3): p. 327-341.
23. Senden, T.J. and C.J. Drummond, *Surface-Chemistry and Tip Sample Interactions in Atomic-Force Microscopy*. *Colloids and Surfaces a-Physicochemical and Engineering Aspects*, 1995. **94**(1): p. 29-51.
24. Israelachvili, J., *Intermolecular and Surface Forces*. 2nd ed. 1991, San Diego: Academic Press. 450.
25. Ninham, B.W. and Parsegia.Va, *Electrostatic Potential between Surfaces Bearing Ionizable Groups in Ionic Equilibrium with Physiologic Saline Solution*. *Journal of Theoretical Biology*, 1971. **31**(3): p. 405.
26. Fleck, C., R.R. Netz, and H.H. von Grunberg, *Poisson-Boltzmann theory for membranes with mobile charged lipids and the pH-dependent interaction of a DNA molecule with a membrane*. *Biophysical Journal*, 2002. **82**(1): p. 76-92.

27. Takano, H., et al., *Chemical and Biochemical Analysis Using Scanning Force Microscopy*. Chemical Reviews, 1999. **99**: p. 2845-2890.
28. Lehenkari, P., et al., *Adapting atomic force microscopy for cell biology*. Ultramicroscopy, 2000. **82**(1-4): p. 289-295.
29. Moy, V., E. Florin, and H. Gaub, *Intermolecular Forces and Energies between Ligands and Receptors*. Science, 1994. **266**(5183): p. 257-259.
30. Florin, E.L., V.T. Moy, and H.E. Gaub, *Adhesion Forces between Individual Ligand-Receptor Pairs*. Science, 1994. **264**(5157): p. 415-417.
31. Hinterdorfer, P., et al., *Detection and localization of individual antibody-antigen recognition events by atomic force microscopy*. Proceedings of the National Academy of Sciences of the United States of America, 1996. **93**(8): p. 3477-3481.
32. Wickremasinghe, N.S. and J.H. Hafner, *Protein crystals as scanned probes for recognition atomic force microscopy*. Nano Letters, 2005. **5**(12): p. 2418-2421.
33. Oberhauser, A.F., et al., *Stepwise unfolding of titin under force-clamp atomic force microscopy*. Proceedings of the National Academy of Sciences of the United States of America, 2001. **98**(2): p. 468-472.
34. Schneider, J., W. Barger, and G.U. Lee, *Nanometer scale surface properties of supported lipid bilayers measured with hydrophobic and hydrophilic atomic force microscope probes*. Langmuir, 2003. **19**(5): p. 1899-1907.
35. Butt, H.J., *Measuring Electrostatic, Vanderwaals, and Hydration Forces in Electrolyte-Solutions with an Atomic Force Microscope*. Biophysical Journal, 1991. **60**(6): p. 1438-1444.

36. Butt, H.J., *Electrostatic Interaction in Atomic Force Microscopy*. Biophysical Journal, 1991. **60**(4): p. 777-785.
37. Ducker, W.A., T.J. Senden, and R.M. Pashley, *Direct Measurement of Colloidal Forces Using an Atomic Force Microscope*. Nature, 1991. **353**(6341): p. 239-241.
38. Ducker, W.A., T.J. Senden, and R.M. Pashley, *Measurement of Forces in Liquids Using a Force Microscope*. Langmuir, 1992. **8**(7): p. 1831-1836.
39. Li, Y.Q., et al., *Direct Measurement of Interaction Forces between Colloidal Particles Using the Scanning Force Microscope*. Langmuir, 1993. **9**(3): p. 637-641.
40. Drummond, C.J. and T.J. Senden, *Examination of the Geometry of Long-Range Tip Sample Interaction in Atomic-Force Microscopy*. Colloids and Surfaces a-Physicochemical and Engineering Aspects, 1994. **87**(3): p. 217-234.
41. Manne, S., et al., *Direct Visualization of Surfactant Hemimicelles by Force Microscopy of the Electrical Double-Layer*. Langmuir, 1994. **10**(12): p. 4409-4413.
42. Rotsch, C. and M. Radmacher, *Mapping local electrostatic forces with the atomic force microscope*. Langmuir, 1997. **13**(10): p. 2825-2832.
43. Heinz, W.F. and J.H. Hoh, *Relative surface charge density mapping with the atomic force microscope*. Biophysical Journal, 1999. **76**(1): p. 528-538.
44. Czajkowsky, D.M., et al., *Direct visualization of surface charge in aqueous solution*. Ultramicroscopy, 1998. **74**(1-2): p. 1-5.
45. Johnson, A.S., et al., *Fluid electric force microscopy for charge density mapping in biological systems*. Langmuir, 2003. **19**(24): p. 10007-10010.

46. Muller, D.J. and A. Engel, *The height of biomolecules measured with the atomic force microscope depends on electrostatic interactions*. Biophysical Journal, 1997. **73**(3): p. 1633-1644.
47. Schneider, J., et al., *Atomic force microscope image contrast mechanisms on supported lipid bilayers*. Biophysical Journal, 2000. **79**(2): p. 1107-1118.
48. Hillier, A.C., S. Kim, and A.J. Bard, *Measurement of double-layer forces at the electrode/electrolyte interface using the atomic force microscope: Potential and anion dependent interactions*. Journal of Physical Chemistry, 1996. **100**(48): p. 18808-18817.
49. Seog, J., et al., *Direct measurement of glycosaminoglycan intermolecular interactions via high-resolution force spectroscopy*. Macromolecules, 2002. **35**(14): p. 5601-5615.
50. Stankovich, J. and S.L. Carnie, *Electrical double layer interaction between dissimilar spherical colloidal particles and between a sphere and a plate: Nonlinear Poisson-Boltzmann theory*. Langmuir, 1996. **12**(6): p. 1453-1461.
51. Fan, T.H. and A.G. Fedorov, *Electrohydrodynamics and surface force analysis in AFM Imaging of a charged, deformable biological membrane in a dilute electrolyte solution*. Langmuir, 2003. **19**(26): p. 10930-10939.
52. Cleveland, J.P., et al., *A nondestructive method for determining the spring constant of cantilevers for scanning force microscopy*. Review of Scientific Instruments, 1993. **64**(2): p. 403-405.

53. Russell, W.B., D.A. Saville, and W.R. Schowalter, *Colloidal Dispersions*. Cambridge Monographs on Mechanics and Applied Mathematics, ed. G.K. Batchelor. 1989, Cambridge: Cambridge University Press.
54. Zhmud, B.V., A. Meurk, and L. Bergstrom, *Evaluation of surface ionization parameters from AFM data*. Journal of Colloid and Interface Science, 1998. **207**(2): p. 332-343.
55. Tocanne, J.F. and J. Teissie, *Ionization of Phospholipids and Phospholipid-Supported Interfacial Lateral Diffusion of Protons in Membrane Model Systems*. Biochimica Et Biophysica Acta, 1990. **1031**(1): p. 111-142.
56. Radler, J.O., et al., *Structure of DNA-cationic liposome complexes: DNA intercalation in multilamellar membranes in distinct interhelical packing regimes*. Science, 1997. **275**(5301): p. 810-814.
57. Salditt, T., et al., *Two-dimensional smectic ordering of linear DNA chains in self-assembled DNA-cationic liposome mixtures*. Physical Review Letters, 1997. **79**(13): p. 2582-2585.
58. Firshein, W., *Role of the DNA Membrane Complex in Prokaryotic DNA-Replication*. Annual Review of Microbiology, 1989. **43**: p. 89-120.
59. Behr, J.P., *Gene-Transfer with Synthetic Cationic Amphiphiles - Prospects for Gene-Therapy*. Bioconjugate Chemistry, 1994. **5**(5): p. 382-389.
60. Verma, I.M. and N. Somia, *Gene therapy - promises, problems and prospects*. Nature, 1997. **389**(6648): p. 239-242.

61. Felgner, J.H., et al., *Enhanced Gene Delivery and Mechanism Studies with a Novel Series of Cationic Lipid Formulations*. Journal of Biological Chemistry, 1994. **269**(4): p. 2550-2561.
62. Templeton, N.S., et al., *Improved DNA: Liposome complexes for increased systemic delivery and gene expression*. Nature Biotechnology, 1997. **15**(7): p. 647-652.
63. Fang, Y. and J. Yang, *Effect of cationic strength and species on 2-D condensation of DNA*. Journal of Physical Chemistry B, 1997. **101**(18): p. 3453-3456.
64. Lasic, D.D., et al., *The structure of DNA-liposome complexes*. Journal of the American Chemical Society, 1997. **119**(4): p. 832-833.
65. Maier, B. and J.O. Radler, *Conformation and self-diffusion of single DNA molecules confined to two dimensions*. Physical Review Letters, 1999. **82**(9): p. 1911-1914.
66. Gelbart, W.M., et al., *DNA-inspired electrostatics*. Physics Today, 2000. **53**(9): p. 38-44.
67. Harries, D., et al., *Structure, stability, and thermodynamics of lamellar DNA-lipid complexes*. Biophysical Journal, 1998. **75**(1): p. 159-173.
68. May, S., D. Harries, and A. Ben-Shaul, *Macroion-induced compositional instability of binary fluid membranes*. Physical Review Letters, 2002. **89**(26): p. -.
69. Harries, D., S. May, and A. Ben-Shaul, *Adsorption of charged macromolecules on mixed fluid membranes*. Colloids and Surfaces a-Physicochemical and Engineering Aspects, 2002. **208**(1-3): p. 41-50.

70. Mbamala, E.C., A. Ben-Shaul, and S. May, *Domain formation induced by the adsorption of charged proteins on mixed lipid membranes*. *Biophysical Journal*, 2005. **88**(3): p. 1702-1714.
71. Fleck, C.C. and R.R. Netz, *Counterion density profiles at charged flexible membranes*. *Physical Review Letters*, 2005. **95**(12): p. -.
72. Franzin, C.M. and P.M. Macdonald, *Polylysine-induced H-2 NMR-observable domains in phosphatidylserine/phosphatidylcholine lipid bilayers*. *Biophysical Journal*, 2001. **81**(6): p. 3346-3362.
73. Carbone, M.A. and P.M. Macdonald, *Cardiotoxin II segregates phosphatidylglycerol from mixtures with phosphatidylcholine: P-31 and H-2 NMR spectroscopic evidence*. *Biochemistry*, 1996. **35**(11): p. 3368-3378.
74. Heimburg, T., B. Angerstein, and D. Marsh, *Binding of peripheral proteins to mixed lipid membranes: Effect of lipid demixing upon binding*. *Biophysical Journal*, 1999. **76**(5): p. 2575-2586.
75. Gawrisch, K., et al., *Role of Interactions at the Lipid-Water Interface for Domain Formation*. *Molecular Membrane Biology*, 1995. **12**(1): p. 83-88.
76. Gambhir, A., et al., *Electrostatic sequestration of PIP2 on phospholipid membranes by basic/aromatic regions of proteins*. *Biophysical Journal*, 2004. **86**(4): p. 2188-2207.
77. Rauch, M.E., et al., *Myristoylated alanine-rich C kinase substrate (MARCKS) sequesters spin-labeled phosphatidylinositol 4,5-bisphosphate in lipid bilayers*. *Journal of Biological Chemistry*, 2002. **277**(16): p. 14068-14076.

78. Xu, W., et al., *Atomic force microscope measurements of long-range forces near lipid-coated surfaces in electrolytes*. *Biophysical Journal*, 1997. **72**(3): p. 1404-1413.
79. Meurk, A., P.F. Luckham, and L. Bergstrom, *Direct Measurement of Repulsive and Attractive van der Waals Forces between Inorganic Materials*. *Langmuir*, 1997. **13**(14): p. 3896-3899.
80. Ashby, P.D., L.W. Chen, and C.M. Lieber, *Probing intermolecular forces and potentials with magnetic feedback chemical force microscopy*. *Journal of the American Chemical Society*, 2000. **122**(39): p. 9467-9472.
81. Dufrene, Y.F., et al., *Characterization of the physical properties of model biomembranes at the nanometer scale with the atomic force microscope*. *Faraday Discussions*, 1998(111): p. 79-94.
82. Israelachvili, J.N., *Strength of Van-Der-Waals Attraction between Lipid Bilayers*. *Langmuir*, 1994. **10**(9): p. 3369-3370.
83. Pera, I., et al., *Using the atomic force microscope to study the interaction between two solid supported lipid bilayers and the influence of synapsin I*. *Biophysical Journal*, 2004. **87**(4): p. 2446-2455.
84. Eisenberg, M., et al., *Adsorption of Mono-Valent Cations to Bilayer Membranes Containing Negative Phospholipids*. *Biochemistry*, 1979. **18**(23): p. 5213-5223.
85. Fleck, C.C. and R.R. Netz, *Counterions at disordered charged planar surfaces*. *Europhysics Letters*, 2005. **70**(3): p. 341-347.
86. Fleck, C.C. and R.R. Netz, *Surfaces with quenched and annealed disordered charge distributions*. *European Physical Journal E*, 2007. **22**(4): p. 261-273.

87. Benda, A., et al., *How To Determine Diffusion Coefficients in Planar Phospholipid Systems by Confocal Fluorescence Correlation Spectroscopy*. *Langmuir*, 2003. **19**(10): p. 4120-4126.
88. Cevc, G., A. Watts, and D. Marsh, *Titration of the Phase-Transition of Phosphatidylserine Bilayer-Membranes - Effects of Ph, Surface Electrostatics, Ion Binding, and Headgroup Hydration*. *Biochemistry*, 1981. **20**(17): p. 4955-4965.